An Initial Study of the Fundamentals of Ice Crystal Icing Physics in the NASA Propulsion Systems Laboratory

Peter M. Struk[1]
Thomas P. Ratvasky[2]
Timothy J. Bencic[3]
Judith F. Van Zante[4]
Michael C. King[5]
NASA Glenn Research Center, Cleveland, OH, 44135

and

Jen-Ching Tsao[6]
Tadas P. Bartkus[7]
Ohio Aerospace Institute, Cleveland, OH 44135

This paper presents results from an initial study of the fundamental physics of ice-crystal ice accretion using the NASA Propulsion Systems Lab (PSL). Ice accretion due to the ingestion of ice-crystals is being attributed to numerous jet-engine power-loss events. The NASA PSL is an altitude jet-engine test facility which has recently added a capability to inject ice particles into the flow. NASA is evaluating whether this facility, in addition to full-engine and motor-driven-rig tests, can be used for more fundamental ice-accretion studies that simulate the different mixed-phase icing conditions along the core flow passage of a turbo-fan engine compressor. The data from such fundamental accretion tests will be used to help develop and validate models of the accretion process. The present study utilized a NACA0012 airfoil. The mixed-phase conditions were generated by partially freezing the liquid-water droplets ejected from the spray bars. This paper presents data regarding (1) the freeze out characteristics of the cloud, (2) changes in aerothermal conditions due to the presence of the cloud, and (3) the ice accretion characteristics observed on the airfoil model. The primary variable in this test was the PSL plenum humidity which was systematically varied for two duct-exit-plane velocities (85 and 135 m/s) as well as two particle size clouds (15 and 50 µm MVDi). The observed clouds ranged from fully glaciated to fully liquid, where the liquid clouds were at least partially supercooled. The air total temperature decreased at the test section when the cloud was activated due to evaporation. The ice accretions observed ranged from sharp arrow-like accretions, characteristic of ice-crystal erosion, to cases with double-horn shapes, characteristic of supercooled water accretions.

Nomenclature

A = Area of test section
AAI = Advanced Aircraft Icing subproject.

[1] Aerospace Engineer, Icing Branch, 21000 Brookpark Road, MS 11-2, AIAA Senior Member
[2] Aerospace Engineer, Icing Branch, 21000 Brookpark Road, MS 11-2, AIAA Senior Member
[3] Optical Specialist, Instrumentation and Controls Div., 21000 Brookpark Rd, MS 77-1, and AIAA Senior Member.
[4] Technical Lead: Icing, Facilities and Test Div., 21000 Brookpark Rd, MS 6-2, and AIAA Senior Member.
[5] Aerospace Engineer, Icing Branch, 21000 Brookpark Road, MS 11-2, AIAA Senior Member.
[6] Principle Research Scientist, Icing Branch, 21000 Brookpark Road, MS 11-2, AIAA Associate Fellow
[7] Senior Research Scientist, Icing Branch, 21000 Brookpark Road, MS 110-3

CDP = Cloud Droplet Probe (by Droplet Measurement Technology, Inc.)
CIP = Cloud Imaging Probe (by Droplet Measurement Technology, Inc.)
ΔGWC_e = Gas water content gained due to evaporation
ICI = Ice crystal icing
IRT = NASA Icing Research Tunnel
$LWC_{m,0.5}$ = Liquid water content, measured using multi-wire probe's 0.5-mm diameter wire
$LWC_{m,2.1}$ = Liquid water content, measured using multi-wire probe's 2.1-mm diameter wire
M = Mach number
m = Leading edge growth rate
$\dot{m}_{noz}$ = mass flow rate of water through a single nozzle
MVD_i = Median volumetric diameter of cloud at spray bar, estimated
NRC = National Research Council of Canada
Nozzles = Number of nozzles
P = Pressure, plenum
$P_{air,noz}$ = Pressure of air supplied to nozzles (differential or gauge pressure)
PSD = Particle size distribution
PSL = NASA Propulsion Systems Lab
P_{tank} = Pressure, tank
$P_{water,noz}$ = Pressure of water supplied to nozzles (differential or gauge pressure)
ΔP_{noz} = Pressure differential, water minus air, = $P_{water,noz}$- $P_{air,noz}$
Q_{noz} = Volumetric flow rate of water provided to each nozzle
RATFac = NRC's Research Altitude Test Facility
RFTP = Reward Facing Temperature Inlet
RH = Relative humidity (%)
RTD = Resistance temperature device
T = Temperature, air
TAT = Total Air Temperature
T_{water} = Temperature, water and air supplied to spray bars
$\Delta T_{0,e}$ = Temperature, delta, cloud on minus cloud off, = $T_{0,e,on}$ - $T_{0,e,off}$
T_{wb} = wet-bulb temperature
TWC_{bulk} = Total water content, bulk, per equation 1
TWC_m = Total water content, measured using multi-wire half pipe
v = Velocity - bulk, test section

Greek Letters

η = Melt ratio defined as max ($LWC_{m,2,1}$, $LWC_{m,0.5}$) / TWC_m
τ = Spray time
ω = Mass mixing ratio
$\Delta\omega_e$ = Mass mixing ratio, test section, delta, ($=\omega_{e,on} - \omega_{e,off}$)
ω_i = Mass mixing ratio, plenum (before spray bars)
ρ = Density, air (dry)

Subscripts

0 = total or plenum conditions
c = corrected to tunnel centerline conditions
e = exit or test section (i.e. PSL station 1) conditions
est = estimated value
i = inlet (at spray bars) condition
off = Cloud-off measurement or calculation
on = Cloud-on measurement or calculation
s = static conditions

I. Introduction

Numerous jet-engine power-loss events are attributed to icing that occurs due to the ingestion of ice-crystals at high altitudes[1]. NASA is investigating the fundamental physical mechanisms of such icing which occurs in core compressor regions of jet engines when ingesting ice crystals. The overarching goal of these tests is to improve understanding of the ice growth physics and expand engine aero-thermodynamic modeling capability to predictively assess the onset and growth of ice in current and future engines during flight. The data from such fundamental accretion tests is helping develop and validate numerical models of the ice-crystal ice accretion process[2-5].

The NASA Propulsions Systems Lab (PSL) has recently added a capability to inject ice particles into an operating jet-engine[6]. To date, a number of successful test programs using both jet engines and test rigs have been performed at the facility offering insight into the engine ice-crystal icing[7, 8]. At PSL, the ice particles are generated using liquid-water spray nozzles which are injected upstream in a plenum area. The water droplets freeze prior to reaching the engine or rig due to a combination of convective and evaporative cooling. Once inside the jet-engine, the ice particles are presumed to break-apart and begin to melt generating a mixed-phase condition before reaching the accretion site in the compressor.

Factors that affect the underlying icing processes included particle impact and breakup, phase change, accretion, and erosion. Furthermore, it is critical to quantify key icing parameters at the accretion site such as the total water content, fraction of liquid to total water content, particle size and phase distribution, and aero-thermal conditions such as pressure, velocity, temperature, and humidity. It is difficult to study the physics of such accretions directly inside the engine. Thus, NASA is evaluating whether the PSL facility, in addition to full-engine and motor-driven-rig tests, can be used for more fundamental ice-accretion studies. These fundamental studies seek to simulate the internal engine conditions leading to icing but in an external flow environment. This necessitates matching the internal environment at the accretion site of the jet engine including the (1) wet-bulb temperature, (2) particle size distribution, and (3) melted portion of incoming ice. A further objective of this research is to develop the capability to generate a prescribed mixed-phase condition at the test section for fundamental ice-crystal icing (ICI) research. Early preparations and preliminary results leading to the present study were reported last year[9].

II. Experimental Description

The present study utilized a NACA0012 airfoil placed at the exit duct of PSL operating as a free jet (Figure 1). The airfoil was located 12.7 cm (5”) aft of the duct exit and geometrically aligned at a zero degree angle-of-attack. For this test, the PSL had a 27:1 area contraction with the exit duct terminating in a 0.91 m (36”) diameter free jet (Figure 2). Two of the available 8 days of testing were dedicated for generating ice accretion data on the airfoil with the remaining 6 days dedicated for cloud characterization. The cloud characterization consisted of spray pattern optimization and uniformity characterization (1 day), mixed-phase generation and measurements (3 days), particle size measurements (1 day), and total water content measurements (1 day). Figure 3 shows each test configuration as viewed from a camera attached to the spray bars in the plenum looking at the exit of the free jet (forward looking aft). The configurations are in the order as they were run during testing.

For these tests, the mixed-phase conditions were generated by partially freezing the liquid-water droplets ejected from the spray bars. Spray bar parameters such as air and water pressures, temperatures, as well as supplemental cooling air were varied to determine the effect on the cloud at the test section (i.e. exit of the free jet as shown in Figure 2). Also, PSL plenum conditions were varied to examine the effects of air temperature, pressure, and humidity on the water droplet freeze-out characteristics.

A. Ice Accretion Hardware & Ice Shape Measurements

The NACA0012 airfoil model has a 266.7 mm (10.5”) chord length and consisted of a center hollow body with solid extensions pieces (Figure 1). The center hollow body is the same airfoil model used in previous testing[10]. That model, which was made from titanium alloy Ti-6Al-4V, has a span of 131.3 cm (5.168”) with the centermost 80.5 mm (3.168”) region being hollow. The hollow region extends 147.3 mm (5.8”) from the leading edge with a wall thickness of 3.2 mm (0.125”). Solid titanium spars of 25.4 mm (1”) spanned both sides of the center hollow region. The span of the model was increased to a total length of 1.012 m (39.825”) by adding solid aluminum airfoil extensions with lengths of 0.437 m (17.188”) on either side of the center hollow body.

1. Surface Temperature Measurements & Heater System

The NACA 0012 airfoil has 14 type K thermocouples embedded in the airfoil surface as shown in Figure 4. An additional thermocouple (#15) is embedded within the center model on the metal surface at the aft end of the hollow air cavity. The table in the figure defines the locations of the thermocouples relative to leading edge at midspan. Measurements from the midspan thermocouples (bolded in the table) are reported in this paper. The thermocouples are flush with the surface and sealed to ensure no air and/or water can penetrate into the body of the airfoil. The epoxy used to fill the holes has the trade name called Artic Silver™.

Each solid airfoil extension had four flexible polyimide heaters attached to the surface of the airfoil. The heaters were 102 x 305 mm (4" x 12") with the longest dimension wrapped symmetrically around the leading edge of the airfoil. Thermocouples were mounted at the leading edge under the heaters. A heater control system maintained the leading edge temperature at a particular setpoint up to the maximum wattage of the heaters. Insulating spacers, 3.18 mm (1/8") thick, made from Garolite and cut to the profile of the NACA0012 thermally isolated the titanium centerbody from the solid aluminum extensions. Aluminum tape, 50.8 mm (2") wide, was placed symmetrically along the leading edge of the airfoil extensions to protect the heaters from possible erosion due to the ice-crystal cloud as seen in Figure 1. In addition, aluminum tape, 25.4 mm (1") wide covered the seams between the airfoil centerbody and extensions as well the fastener holes on the aft end of the model.

2. Ice Accretion Measurements

Only the middle 80.5 mm (3.168") span of the airfoil – the titanium center hollow body - was intended for ice accretion characterization with the airfoil extensions covered by surface heaters. Tests were performed with and without surface heaters activated. In some cases, the surface heaters were not able to keep the airfoil deiced. In several such cases, the surface heaters would cause a portions of the ice accretion to shed resulting in an undesired asymmetric growth. For the test cases presented in this paper, the heater system was not active.

Video cameras, placed outside the flow, provided various perspectives of the airfoil to image ice accretion. The cameras (Sony model FCB-H11) produced high-definition images at resolutions of 1280 by 720 pixels at 59.94 Hz. Figure 13 and later shows images from the video taken using a side and top-down view of the airfoil. The side view camera produces a backlit image of the ice profile at the maximum thickness allowing a 2D ice shape profile to be extracted using image analysis software. Since the magnification of the ice shape changes at different distances from the camera (i.e. perspective effect), small ice accretions (< 2 mm thickness) were not visible at midspan from the side view camera. The top-view camera images are used to gauge the location of the maximum span-wise thickness. Image analysis software measured the leading edge ice thickness at midspan from the top-view. This paper presents only leading-edge ice thickness measurements with the 2D ice profile shapes planned for future comparisons to ice accretion code predictions.

B. Test Matrix and Target Conditions

While there were many objectives of the first fundamental ice-crystal icing test at PSL, this paper focuses on four plenum humidity sweeps conducted at two different velocities and two initial spray bar settings with the remaining conditions constant. The target plenum relative humidity, $RH_{i,0,T}$ (subscripts denoting inlet plane, total conditions, and target, respectively) were set to discrete values ranging from approximately 0 to 60%. Generally, the test sequence started with the $RH_{i,0,T}$ in the middle of the range. Subsequent tests both lowered and increased the *RH* until the cloud was completely glaciated or fully liquid, respectively. The flow velocities, $v_{e,T}$, were 85 and 135 m/s while the spray bar settings were set to produce initial particle size distributions, MVD_i, of 15 and 50 µm (discussed further below). The other target facility conditions were kept constant at $P_{0,i,T}$ = 44.8 kPa (6.5 psia) and $T_{0,i,T}$ = 7.2°C with a static pressure of 42.8 kPa (6.2 psia) and 40.0 kPa (5.8 psia) for the 85 and 135 m/s cases, respectively. The targeted total water content at the test section was 2 g/m^3 assuming the water was uniformly distributed across a 61-cm (24 inch) diameter circle. However, the water content was later estimated to be higher due to the spray bar patterns used as discussed in the next section.

1. Setting Water Content

The bulk total water content (TWC_{bulk}) at the test section was set using equation 1 below. In this equation $\dot{m}_{noz}$ is the mass flow rate through a single nozzle, *Nozzles* is the number of spray nozzles used to generate the cloud, v_e is the calculated air flow velocity at the test section, and *A* is the cloud effective area. TWC_{bulk} shown in Eq. 1 assumes that all of the injected water is uniformly distributed across the effective cloud area. In preparation for this test, the

targeted TWC_{bulk} of 2 g/m^3 used an A based on a 61.0 cm (24") diameter circle. However, the effective area was later adjusted after some data analysis and is discussed subsequently.

$$TWC_{bulk} = \frac{(\mathrm{N}ozzles)\,\dot{m}_{noz}}{v_e A} \tag{1}$$

During the first day of testing, different spray bar nozzle patterns were tested with the goal of keeping all of the water within the innermost 61.0 cm (24") diameter of the PSL exit duct and to generate a uniform cloud across the middle 15 cm (~6") of the cloud. The water patterns were gauged using the PSL tomography system[11, 12]. After some limited experimentation, the nozzle patterns selected for the standard and mod-1 nozzles are shown in Figure 6. A total of 22 and 19 nozzles were selected from the standard and mod-1 set, respectively. A larger number of standard nozzles were required to achieve the desired TWC values at the higher flow speeds. These spray bar patterns were used through the remainder of the test.

Figure 6 shows elliptical regions superimposed on the selected nozzle patterns. These elliptical regions represent the geometrical height and width of the physical spray bar pattern plus a constant 11.9 cm (4.7") increase due to spray expansion. The spray expansion increase was based on data from images of the spray taken at the NASA IRT which suggest the geometric spray expansion was insensitive to spray bar pressure settings. The resulting spray diameter at the plenum just downstream of the nozzles is then 1.78 m which is the equivalent circular diameter of the ellipse.

Assuming that this spray pattern remains largely intact as it transitions from the plenum to the test section suggests that the effective area A of the cloud to use for Eq. (1) should use a diameter of 33.94 cm (13.36") instead of the 61.0 cm (24") diameter initially assumed. This spray diameter at the test section is calculated by taking the ratio of spray diameter to plenum diameter and scaling it to the test section diameter (i.e. 1.78 m / 4.794 m * 91.4 cm). Using this new A, the TWC_{bulk} increases from 2 g/m^3 to 6.5 g/m^3.

When running the actual tests, the air flow velocity at the test section, v_e, was often slightly less than the target value due to blockage effects from the probes. As a result, the TWC_{bulk} further increased (for example, the 6.5 g/m^3 typically became about 6.8 g/m^3). The TWC_{bulk} values presented in this paper are these larger values based on the nozzle pattern areas and the air velocity based on as-measured conditions.

Some resulting water distribution patterns from the PSL tomography system are shown in Figure 7. These images are 512 by 512 pixel and show approximately 30 second averages of the spray pattern. There are 3 circles superimposed onto the images with diameters of 61.0 cm (24"), 76.2 cm (30)", and 91.4 cm (36"). The inner most diameter was the target diameter to keep all water within. The middle diameter is the extent of tomography sensitivity. The largest diameter circle represents the duct wall. Figure 7A & B shows patterns from the 85 m/s cases while Figure 7C & D show 135 m/s cases. The primary differences in Figure 7A & B are the particle size distributions for the cloud (similarly for Figure 7C & D) as well as the target plenum humidity. For all of the cases, the intensity measurements suggest that the bulk of the water was well within the target 61.0 cm (24") diameter corroborating the use of a smaller cloud effective area in eq. (1).

During post processing, the tomography image intensity is scaled such that the center 2.54 cm (1") square (7 pixel by 7 pixel) average is set equal to unity. Since the peak intensity was typically not precisely at the center of the duct, intensity regions greater than 1 appear as seen in several of the images in Figure 7. In the analysis, only pixels with an intensity value of 0.01 or greater are counted and intensity values below this threshold are set to zero to eliminate image noise. Each image in the figure shows a concentration factor (CF) value in the lower right corner. The CF is the ratio of average intensity across the middle 2.54 cm (1") square to the average intensity across the 61.0 cm (24") circular diameter. The ratio, CF+, uses only pixels with an intensity value greater than 0.01 while CF uses all pixels. The other 2.54 x 2.54 cm (1" x 1") square area regions overlaid in the image represent the locations of various probes during testing showing that several of the instruments were in the periphery of the cloud.

2. Setting Particle Size

The PSL spray bars have the same types of nozzles as installed in the NASA Icing Research Tunnel (IRT). At IRT, only a small amount of evaporation occurs between the spray bars and the test section due to nearly saturated air conditions. Hence, an assumption is made that the particle size distributions (PSDs) at the IRT test section are the same as near the spray nozzle plane. As a result, the PSD at the PSL spray bars is approximated to be the IRT values for the same supplied water and air pressures[13]. In this paper, a particular spray PSD is referred to by the IRT mean volumetric diameter and is given the subscript "i" to denote the inlet plane (MVD_i).

As they flow from the spray bars to the test section, the droplets evaporate and reduce in size with the smallest droplet possibly evaporating completely. Furthermore, the rates of evaporation are expected to vary with different test conditions such as temperature, pressure, and local humidity resulting in different particle size distribution for the same spray bar settings. Various instruments made measurements of the PSDs at or near the duct exit plane. The measurements are described in a subsequent section.

C. Measurements

Measurements of air temperature, pressure, and humidity were made at various locations in the plenum and at the test section. This section gives some details of those measurements. All plenum measurement results presented in this paper are averages for the duration of the spray. Measurement of temperature and humidity at the test section include cloud off and cloud on values which are 30-second averages of the particular parameter just prior to initiating and stopping a spray, respectively. The cloud-on data is reported as a change (i.e. delta) from the cloud-off measurement. The cloud-on temperature and humidity measurements at the test section were adjusted to centerline values as discussed in the uniformity section below. In addition, the cloud-on measurements were adjust for any drift that occurred in the plenum. For instance, if the plenum temperature increased by 0.5°C during the spray compared with the pre-spray (cloud-off) value, then the reported cloud-on temperature change was decreased by 0.5°C. This adjustment is required to make a direct cloud-off versus cloud-on comparison.

1. Temperature

The PSL facility measures the flow total temperature ($T_{0,i}$) using the average of 17 type-K thermocouples mounted just upstream of the spray bar in the plenum. The thermocouples are distributed along the horizontal and vertical diameters of the PSL plenum just upstream of the spray bars. At the test section, air temperature measurements were made using both a commercial total air temperature (TAT) probe and a custom TAT probe (Figure 5). The commercial probe was model 102LJ2AG manufactured by UTC Aerospace Systems which has recently been modified by the manufacturer for better performance in icing conditions. The commercial probe temperature data was adjusted for recovery factor and deicing heat, which was active during testing, using manufacture provided corrections. The custom reward facing TAT probe (RFTP) uses a resistance temperature detector (RTD) placed inside a rearward facing inlet to prevent measurement contamination from impinging water and ice particles. A small suction flow was induced in the custom probe to improve the probe's time response to changes in air temperature. The temperature measurements using the RFTP have been calibrated to read total temperature given the flow Mach number. Generally, both temperature probes measured similarly during cloud-off conditions. During cloud-on conditions, the probes measured similar trends although the actual air temperature measurements differed. However, if the deice heat correction was not applied to commercial TAT measurement during icing conditions then the probes read similarly. Further work is required to understand these differences and is beyond the scope of this paper. Since the deice heat corrections for the commercial TAT probe were quite large at the lower speeds of the current test, the temperature data at the test section reported in this paper are from the RFTP which, at present, are believed to be the more accurate values.

Not all temperature probes were used in all configurations – see Figure 3 for a definition of which probes were used during a particular configuration. Also, the commercial TAT probe changed location in configuration 4. During the first day of testing (configuration 0, Figure 3A), a longer version of the RFTP was used to measure temperature at different radial locations in the cloud which is further discussed below.

2. Humidity

PSL uses the Water Vapor Sensing System (model WVSS-II) manufactured by SpectraSensors, Inc to measure local water vapor content. This instrument uses laser absorption spectroscopy to measure the water vapor content of a continuous flow sample. The continuous sample is extracted via a vacuum driven flow control system connected to the exhaust side of the instrument. The volume flow rate of the continuous sample is controlled to typical values between 5-10 liters per minute through an approximately 6 m (20 feet), 13 mm (½ inch) diameter line.

Three different humidity measurement locations were used during this test: one in the plenum and two near the test section. The plenum inlet is located on the upper wall of the plenum upstream of the spray bars. The test section humidity inlet locations are shown in Figure 3. Humidity inlet A was 6.4 mm (0.25") OD / XX" ID stainless-steel tube with a 90° bend. The bend was aft facing to minimize the possibility of ingesting water and ice during testing. However, contamination due to ingested water did occur in configuration 1 resulting in the addition of a deflector

cone to humidity inlet A for configurations 2 and 3. Unfortunately, contamination still continued to occur occasionally for humidity inlet A and data from this inlet is not included in this report. The contamination was suspected to occur due to accumulation of water somewhere near the inlet port. Humidity inlet B is a rearward facing aerosol inlet adapted for use as a humidity inlet. Starting with the second day of testing in configuration #1, the aft end of humidity inlet B was extended using a Teflon extension tube which prevented liquid water from accumulating near the inlet (see inset image in Figure 3B). All humidity data at the test section reported in this paper comes from humidity inlet B. Humidity inlet B was approximately 245 mm (9.65 inches) from the centerline.

3. Pressure, Velocity, and Mach Number

Three PSL facility pressures are reported in the paper: total pressure ($P_{0,i}$), station 1 static pressure ($P_{s,e}$), and tank pressure (P_{tank}). The total pressure is measured in the plenum while the static pressure is measured via a static wall taps located in the constant area duct upstream of the duct exit plane. The tank pressure is far-field pressure measurement. The Mach number (M) at the duct exit plane is calculated using the pressure measurements $P_{0,i \text{ and }} P_{s,e}$ assuming isentropic flow.

4. Uniformity Measurement (traversing) and Estimate of Centerline Conditions

During early preparatory work for this test[9], radial variations in both temperature and humidity were measured in the presence of the cloud. As a result, the rearward facing inlet used for temperature and humidity measurements was traversed along a radius at the duct exit plane during the first day of testing in configuration 0 (Figure 3A). Traverses were performed for 3 test conditions with the target conditions provided in Table 1 below. The values for total temperature and total relative humidity are pre-spray values. The target values for TWC_{bulk} were initially 2, 2, and 6.5 g/m^3, respectively, but have been adjusted to the values listed in in Table 1 as discussed in section II.B.1.

Table 1. Table of target conditions for the 3 traverse tests.

Escort #	v_T m/s	$P_{0,T}$ kPA	$T_{0,T}$ K	$RH_{0,i}$ %	MVD_i μm	TWC_{bulk} g/m^3	Nozzle Type	Nozzles #
31	85	44.5	280.4	45	15	6.5	Mod 1	19
35	135	87.1	280.4	45	50	6.5	Mod 1	19
39	85	44.5	280.4	45	50	28.0	Standard	22

The measured changes in mixed mass ratio (humidity), $\Delta\omega_e$, and temperature, ΔT_e, between spray on and spray off conditions for several discrete radial locations are shown in Figure 8A & B, respectively. The temperature decreases and humidity increase with the greatest changes occurring at the tunnel centerline. For the lower speed of 85 m/s, the maximum change in air temperature is a decrease of about 5.5 °C with a corresponding humidity increase of 1.6 g/kg. At the higher speed of 135 m/s, the temperature and humidity changes were smaller, a 2.2 °C decrease and 0.7 g/kg increase, respectively. The substantial increase in TWC_{bulk} between Escort[8] #31 and #35 only produced a slightly larger changes in temperature and humidity.

In configurations 1 - 4 (Figure 3B-F), the humidity and temperature measurements were offset from the centerline by approximately 0.25 m (9.65 in). Using data from the traverse tests, a method was formulated to extrapolate the off-center measurements to approximate centerline values. The traverse profiles shared similar non-dimensional characteristics (Figure 9). The non-dimensionalized changes in humidity and temperature are combined in these figures into a single profile. The collapse of the profiles suggest that the non-dimensional profiles are relatively insensitive to exit velocity, air pressure, initial particle distribution size and total water content for the ranges tested. For this work, we use this similarity to estimate centerline conditions when making off-center measurements.

To formulate an expression for these measured changes, the temperature and humidity changes were normalized by the maximum value, $\Delta T_{e,max}$ or $\Delta\omega_{e,max}$, respectively, for each radial traverse. Equation (2) shows a generic non-dimensional value Y, equal to the measured change, Δy, divided by the maximum measured change, Δy_{max}. Radial values were non-dimensionalized by the radial location where the change in Δy is one half the maximum value.

[8] Escort refers to the PSL data acquisition system and specific tests are typically referred to by an "Escort number."

Equation (3) shows the generic form where the non-dimensional radial value, X, is equal to a radial location, x, and the location of half the maximum change, $x_{0.5}$.

The $x_{0.5}$ location for each traverse is listed below in Table 2. The half max location for ΔT is labeled as $x_{0.5,\Delta T}$, while the half max location for $\Delta\omega_e$ is labeled as $x_{0.5,\Delta\omega}$. For the majority tests, there were two exit velocities and two nozzle configurations that were run, giving a total of 4 different combinations. The fourth row shown in Table 2 is an approximation to a condition not tested. The half max locations for this fourth row are approximated by taking a similarity ratio using the 3 radial traverse tests (i.e. 8.318 / 11.794 x 13.754 = 9.700).

Table 2. A table providing the $x_{0.5}$ values for ΔT and ΔMMR for the 3 radial profile tests, along with a 4th interpolation condition.

Escort / Condition	v_T	Nozzle Type	Nozzles	$X_{0.5,\Delta T}$	$X_{0.5,\Delta\omega}$
# / #	m/s		#	cm (inch)	cm (inch)
31 / 106	85	Mod 1	19	4.64 (11.794)	3.87 (9.828)
35 / 108	135	Mod 1	19	3.27 (8.318)	3.46 (8.798)
39 / 109	85	Standard	22	5.41 (13.754)	4.16 (10.571)
Interpolation	135	Standard	22	3.82 (9.700)	3.73 (9.463)

Using the generic non-dimensional values of Y and X, curve fits are applied to the data with the form as expressed in Eq. (4). In this expression, the constant *c* is set to unity as it is approximated that the radial profiles are symmetric along the center axis of the tunnel. The constants *a* and *p* are determined using a least-squares fit to the appropriate data set. The values for the constants are shown in Table 3. Plots of the curve fits are included in Figure 9. Using Eq. (4) along with the appropriate constants from Table 3 and half max location values from Table 2, we can estimate the centerline value Δy_{max} (i.e. either ΔT_{max} or $\Delta\omega_{max}$) with a measurement that is taken at any distance from the centerline, provided the test was in one of the 2 nozzle configurations or exit velocities listed in Table 2. Values that are corrected to centerline conditions using this method are given the subscript "C".

$$Y = \frac{\Delta y}{\Delta y_{max}} = \frac{\Delta T}{\Delta T_{max}} \text{ or } \frac{\Delta\omega}{\Delta\omega_{max}} \tag{2}$$

$$X = \frac{x}{x_{0.5}} \tag{3}$$

$$Y = c\, e^{-aX^p} \tag{4}$$

Table 3. Constants for Eq. 3 and Eq. 4.

TP#	a	c	p
106 & 108	0.68	1	3.5
109	0.68	1	2.51

5. Total Water Content (Isokinetic Probe)

The Isokinetic Total Water Content Evaporator Version 2 (IKP2)[14] made measurements of total water content during configuration 4 of the testing (see Figure 3F). The IKP2 ingests cloud hydrometeors (i.e. particles of liquid water and ice) into an inlet which are then heated to evaporation and then measures the total humidity of the background + evaporated water. The TWC from the ingested hydrometeors is then deduced by subtracting an independent measurement of background humidity. After the first day of testing suggested some non-uniformity of the cloud-on humidity profile across the test section, it was desired to make the background humidity measurement as close to the centerline as possible. For these tests, the background humidity was measured 6" below and 8" aft of IKP inlet. The background humidity inlet was a simple bent stainless-steel tube, 6.4 mm (0.25") OD / XX" ID. A cone was attached to tube upstream of the inlet to help deflect particles to help prevent contamination from ingested water. However, the background humidity values did not always come back immediately to pre-spray values, typically by a

constant small offset, suggesting a small amount of contamination still occurred. During post-processing, the small offset was subtracted from the background humidity before being used in the calculation of TWC.

6. Liquid Water Content (Multiwire Probe) and Calculated Melt Ratio.

The SEA multi-wire probe[15-17] makes measurements of the total and liquid water contents at the test section. The probe provides three different water-content measurements: a total water content measurement using a half-pipe shape element ($TWC_{m,HP}$) and two measurements of liquid water content, $LWC_{m,2.1}$ and $LWC_{m,0.5}$, from two different diameter elements, a 2.1-mm and 0.5-mm diameter element, respectively. Only the LWC values from the larger 2.1-mm diameter element are used in the current work although all measurements from the multiwire are reported.

The melt ratio, n_e, or ratio of liquid to total water content, Eq. (5), is estimated from the measured values of LWC_m and TWC_m. The subscript *m* is used to denote a measured values of water content whereas parameters without a subscript denote an estimate of the actual values. For total water content, the unmodified measurement from the IKP2 is used (i.e. $TWC_m = TWC$) and is assumed to be a simple sum of the *LWC* and *IWC* as shown in Eqs. (5) & (6). For liquid water content, the measured LWC_m from the multiwire is a combination of both impinging liquid and ice. In a purely glaciated cloud, the impinging ice crystal provide a non-zero measurement on the LWC elements which is termed a false response. Here, the false response is assumed to be proportional to IWC with the constant of proportionality label FR for false response as shown in Eq. (7). In a purely liquid cloud, the measured $LWC_m$is less than what is measured by the IKP2. Hence a water catch (WC) efficiency term is applied to the actual LWC as seen in Eq. (7). Finally, the smallest water / ice particles may miss the hot wire altogether which is accounted for the collision efficiency, $CE_{2.1}$. The actual LWC and IWC are then calculated by solving Eq. (6) and (7) simultaneously. Estimates of FR and WC are provided in the results based on data taken during this test and are listed in the appendix as well as the calculated $CE_{2.1}$. It is assumed that both FR and WC remain constant for a given airspeed, pressure, and particle size distribution. However, it is possible that these values may also vary due to the amount of LWC and IWC but decoupling these effects was beyond the scope of the present work.

$$n_e = \frac{LWC}{TWC} = \frac{LWC}{LWC + IWC} \tag{5}$$

$$TWC_{m,IKP} = TWC = LWC + IWC \tag{6}$$

$$LWC_{m,2.1} = CE_{2.1}(WC \cdot LWC + FR \cdot IWC) \tag{7}$$

7. Particle Size Measurements

Particle size measurements were made using the Droplet Measurement Technologies' Cloud Droplet Probe (CDP), which can measure droplet sizes ranging from 2 to 50 µm, and the Cloud Imaging Probe (CIP) - Grey Scale, for sizes ranging from 15 to 960 µm. The CDP and CIP were used in configurations 3a and 3b, respectively. In addition, particle size data was collected using the modular versions of the High Speed Imager (HSI) and Phase-Doppler Interferometer (PDI) probes being developed by Artium Inc. for measurements in mixed-phase clouds. The HSI and PDI were used during configurations 1, 2, and 3a. The HSI and PDI hardware are visible for configuration 2 in Figure 1. The sample volumes for the HSI and PDI were either 15 cm (~6") above or below the tunnel centerline as shown in Figure 3. The PDI data for clouds with ice crystals is still developmental and consequently has a higher uncertainty.

For this paper, a particular cloud particle size distribution (i.e. spray bar condition) is referred to by an MVD_i as described previously. For the smaller particle size clouds (MVD_i = 15 µm), the CDP and PDI results are resported since these instruments are more sensitive to smaller particles. For the larger particle size clouds (MVD_i = 50 µm), the HSI and PDI are reported. The CIP data was not used as the probe number density values were too large and saturated the instrument. The measured d_v50 (i.e. *MVD*) and d_v10 and d_v90 values, when available, are listed in the appendix. The particle size data from the HSI and PDI represent values from combined tests taken on different days and configurations but during the same condition. More details on the HSI and PDI measurements, as well as the full particle spectra, are reported in a separate paper of this conference[18].

III. Results

While there were many objectives of the first fundamental ice-crystal icing test at PSL, the data presented will focus on a series of tests where the plenum humidity was varied systematically while all other aerothermal and spray bar parameters were held constant. The results will focus on the conditions at the test section (duct exit plane) namely (1) the freeze out characteristics of the cloud, (2) changes in aerothermal conditions due to the presence of the cloud, and (3) the ice accretion characteristics observed. The results section uses facility target conditions when describing aerothermal and spray bar settings. The actual, as-measured, values are listed in the appendix.

A. Cloud Freeze-out Characteristics via Changes in Plenum Humidity Sweeps at an Above Freezing Total Temperature

The effect of humidity on the freeze out of the cloud was examined through several plenum humidity sweeps. Lower plenum humidity would enhance evaporation hence evaporative cooling and help promote freeze out. Figure 10 shows water content measurements for four humidity sweeps. The sweeps were performed at two different target velocities, $v_T = 85$ m/s (Figure 10A & B) and 135 m/s (Figure 10C & D), and two different initial particle size distribution, $MVD_i = 15$ µm (Figure 10A & C) and 50 µm (Figure 10B & D). The other target facility conditions were kept constant at $P_{0,i,T}$ = 44.8 kPa (6.5 psia) and $T_{0,i,T}$ = 7.2°C with a static pressure of 42.8 kPa (6.21 psia) and 40.0 kPa (5.8 psia) for the 85 and 135 m/s cases, respectively. At the time of testing, the targeted water content at station-1 was 2 g/m^3 assuming the water was uniformly distributed across a 61-cm (24 inch) diameter circle. However, the injected water content was later estimated to be closer to 6.5 g/m^3 based on the spray bar patterns used in the test as described previously.

Each graph in Figure 10 shows measurements of TWC from the IKP2 ($TWC_{m,IKP2}$) and multiwire probe ($TWC_{m,HP}$, $LWC_{m,2.1}$ and $LWC_{m,0.5}$). Direct measurements from the IKP2 are shown in solid green symbols (◆) while estimated values ($TWC_{est,IKP2}$) are shown in open green symbol (◇). The estimated values were interpolated values from a linear curve fit to the measured data. The linear curve fit to the IKP data is shown in Figure 10. The estimated values were calculated for points not measured during testing but were required for the melt ratio estimate.

As the plenum humidity is increased, the measured TWC for both the IKP and multiwire generally increase although the magnitude of the measurements vary drastically based on the initial velocity and particle size. For the lower speed tests ($v_T = 85$ m/s), the measured $TWC_{m,IKP2}$ across the humidity sweep ranges from about 1 to 2.5 g/m^3 (Figure 10A) with the smaller initial particle size ($MVD_i = 15$ µm) but the range increases from roughly 3 to 5 g/m^3 (Figure 10B) with the larger initial particle size ($MVD_i = 50$ µm). For the higher velocity tests ($v_T = 135$ m/s), the $TWC_{m,IKP2}$ ranges are larger from about 2 to 3.5 g/m^3 (Figure 10C) and 6.5 to 8 g/m^3 (Figure 10D) for the smaller and larger initial particle sizes, respectively.

For each humidity sweep, the degree of cloud freeze out was gauged by the LWC measurements from the multiwire. In all cases, the measurements of $LWC_{m,2.1}$ and $LWC_{m,0.5}$ suggest more freeze out at lower plenum humidity values. For the $MVD_i = 15$ µm cases (Figure 10A & C), there was an abrupt increase in measured LWC between when the plenum relative humidity increased from 30 to 40%. This was noticed immediately during testing and, as a result, test points were added to better refine that boundary. In one case (escort #47), the measured LWC was much lower than a similar test (escort #85.1). In review of the actual measured tests conditions, the tunnel total temperature in the plenum for escort #47 was colder by about 0.5°C compared with escort #85.1 which may explain why that cloud had more freeze out. For the $MVD_i = 50$ µm cases (Figure 10B & D), the transition from ice to liquid was more gradual. Also with the $MVD_i = 50$ µm cases, complete freeze out was not achieved even at a plenum relative humidity of 0% at the warm plenum total temperatures of ~7°C used in this test.

Figure 10 also shows estimates of the false response (*FR*) and water catch (*WC*) efficiency used in this paper to adjust the *LWC* measurements in Eq. (7). The FR data came from the lowest plenum relative humidity values tested where fully glaciated clouds were observed. For the MVD_i = 15 µm cases, the *FR* values increased with airspeed from about 6.6 % at 85 m/s to 13.3% at 135 m/s. Since the MVD_i = 50 µm cases did not freezeout, the *FR* for these cases is approximated as those from the MVD_i = 15 µm cases. The *WC* values came from the highest plenum relative humidity tests where fully liquid conditions were observed. The *WC* value decreased with increasing airspeed. For the MVD_i = 15 µm cases, the *WC* values decreased from 72.2% at 85 m/s to 60.7% at 135 m/s. At MVD_i = 50 µm, the WC decreased from 65.4% at 85 m/s to 47.8% at 135 m/s. The values of *FR* and *WC* apply only to the 2.1-mm multiwire element at these tested conditions.

Finally, Figure 10 denotes where the cloud appeared completed glaciated (i.e. ice) or completely liquid based on observations of ice accretion on the RFTP and humidity inlet (Figure 6) in the tunnel during configuration 1. However, these observations may not be completely accurate indicators of cloud glaciation since the probes were not at the tunnel centerline and there was at least one condition[9] (#309) where the probes showed some ice accretion (escort 89) but the airfoil did accrete ice (escort 147). Finally, the figure also shows which cases were tested with the airfoil in configuration 2 – see blue bar near the bottom of each graph. The letters in the blue bar will be referred to later in this paper to cross-reference conditions – cases where an asterisk is shown in lieu of a letter indicates a test performed with the airfoil but which did not accrete ice.

B. Changes in cloud aero-thermal conditions

Figure 11 shows measured changes in air temperature and humidity (reported as gas water content) at the duct exit plane after the cloud is activated. The reported changes are the differences in 30-second averages of measurements just prior to the cloud coming on and off. The values are corrected for any drift in plenum conditions and adjusted to centerline conditions, as described previously. Figure 11A & B correspond to $v_T = 85$ m/s while Figure 11C & D correspond to 135 m/s. As in the previous figure, the MVD_i is 15 µm in the left column (Figure 11A & C) and 50 µm in the right column (Figure 11B & D). In each graph, the ranges for each axis are the same so direct comparisons can be made. Just as in Figure 10, Figure 11includes the ice accretion reference letters in the blue bar below each graph for reference.

In all cases, the changes in air temperature and humidity is greatest when the plenum humidity is the lowest. As the plenum humidity is increased less evaporation occurs and the changes in air temperature and humidity at the duct exit plane decrease. Regarding temperature, the changes are similar for both the 15 and 50 µm MVD_i for the 85 m/s cases (Figure 11A & B). At a plenum relative humidity of 20%, the air temperature cools about 4°C. When the plenum relative humidity is 60%, the air temperature only cools by about a 2.5 °C. Similar magnitude air temperature changes were observed for the 135 m/s cases and 50 µm MVD_i cloud (Figure 11D). However, the 135 m/s and 15 µm MVD_i cloud cooled significantly more - at a plenum relative humidity of 25%, the air temperature cooled by almost 8 °C. Regarding humidity, the changes were similar in magnitude for the 85 m/s cases with more evaporation occurring with the smaller MVD_i cloud. For instance, at a plenum relative humidity of 20% the gas water content increases by 1.4 g/m^3 for the 15 MVD_i cloud while only increasing by 1.0 g/m^3 for the and 50 µm MVD_i cloud. Similar trends are seen with the 135 m/s cases, as well.

Figure 12 shows the calculated wet-bulb temperature (T_{wb}) for all of the cases from the plenum humidity sweeps. The T_{wb} was calculated using the method described in Veres, et al.[19] and requires an air temperature measurement (i.e. dry-bulb), pressure, and humidity. The T_{wb} calculations using total and static temperature and pressure are denoted with a subscript 0 and s, respectively. All calculations are made using measurements at the duct exit plane, hence the subscript e. In addition, calculations are made with both cloud-off (i.e. pre-spray) and cloud-on measurement (using the average data 30 seconds prior to the termination of the spray when conditions were generally steady). The temperature measurements used were those corrected to tunnel centerline conditions, denoted with a subscript c, as described previously.

The T_{wb} increased with initial plenum humidity as seen in Figure 12. For the slower speed cases of 85 m/s (Figure 12A & B), both the total and static T_{wb} pass through the freezing point as the plenum relative humidity increases above 50%. For the higher speed cases of 135 m/s, only the T_{wb} based on the total temperature increased above freezing. The large drop in static temperature due to the PSL contraction ensured T_{wb} stayed below freezing for these cases. Finally, the cloud-off and cloud-on T_{wb} matched to within 1°C or better as can be seen by comparing the open and closed symbols in Figure 12.

Additionally, Figure 12 also shows an estimate of the melt ratio at the duct exit plane, η_e, for all of the cases of the plenum humidity sweeps. The method for estimating η_e is described previously in section II.C.6. The estimates of η_e show cloud conditions ranging from fully-glaciated to fully liquid. A fully glaciated cloud occurred at the lowest plenum humidity values only for the smaller MVD_i of 15 µm for both the 85 and 135 m/s cases (Figures 12A and C). For the larger MVD_i of 50 µm, a mixed-phase cloud occurred even at the lowest plenum relative humidity of ~0% for both velocity cases (Figures 12A and C). In these cases, modelling work presented in a separate complementary

[9] Condition numbers (CN) refer to a particular aero-thermal and spray bar setting. Conditions were repeated during the various configurations of the test. Escort numbers refer to an actual spray that occurred using a particular condition.

paper[20] suggests that the larger droplets do not have sufficient time to freeze. The clouds were estimated to be fully liquid or nearly fully liquid for the higher plenum relative humidity values. Ice accretion generally occurred for most of the lower (non-zero) η_e values although ice accretion was observed for a few of the higher η_e values.

C. Ice accretion characteristics

Tests with the airfoil (configuration 2) were performed for a subset of the plenum relative humidity tests referenced in Figures 10-12. In these figures, the letters in the blue bar at the bottom of each graph denotes a condition which was tested and accreted ice. Cases where an asterisk is shown indicates an airfoil test but which did not accrete ice. There are a total of 8 ice accretions presented, labelled accretion "a" through "h". Images from these accretions are presented followed by midspan ice thickness and surface thermocouple measurements versus time. For each accretion, images at two different times are shown: one earlier in the spray, after about180 seconds of cloud exposure, and one at the end of the spray, after approximately 600 seconds of cloud exposure. Both a side and top view image of the ice accretion is shown. During testing the camera zoom was adjusted so the field of view may vary from image to image. For all of the cases presented, there was no deicing heat applied to the airfoil extensions.

Following the images for a particular ice accretion are measurements of ice thickness and surface thermocouple measurements versus time from the start of the spray. The ice thickness is measured at the model midspan from the top-view camera. The surface temperature measurements are those from thermocouples distributed along the model centerline from the leading edge to just over mid-chord. The locations of the thermocouples are defined in Figure 4.

Figures 13-14 show data from ice accretion "a" which occurred at a $v_T = 85$ m/s, a 15 μm MVD_i, and a plenum relative humidity of 40%. From the top view camera, this accretion had a glazy appearance with small feather-like features. Early in the spray, a small layer of ice was observed to occur just aft of the leading edge extending a few cm back. Between 180 and 600 seconds of cloud exposure, the ice accretion grew further aft but was limited to the center hollow-portion of the model with no accretion visible on the solid airfoil extensions. This ice accretion did not have any appreciable thickness (< 2 mm) and was not visible from the side view camera (Figure 14A) due to a perspective effect described previously. The thermocouple traces seen in Figure 14B show the surface temperature cooling down more quickly nearer the leading edge. All of the thermocouples eventually reach 0°C including the aft-most thermocouple (TC14) although it takes almost 6 minutes to reach that temperature.

Figures 15-17 show data from ice accretions "b" through "e" which all occurred at $v_T = 85$ m/s and 50 μm MVD_i but with different plenum relative humidity values. Figures 15 and 16 show images from 180 and 600 seconds of cloud exposure, respectively. After 180 seconds, ice accretions "b", "c", and "d" all have similar leading-edge thickness. From the side view images, ice accretion "b" has less feather-like features compared to accretions "c" and "d". Also, accretion "b" has a small elevated ridge near the stagnation line. From the top-view images, accretions "b" and "c" extend onto the solid airfoil extensions while accretions "d" and "e" were primarily on the center hollow-portion of the model. Ice accretion "e" only started to grow measurably after approximately 300 seconds. The ice accretions after ~600 seconds of exposure (Figure 16) showed noticeably different characteristics. Both accretions "b" and "c" had a more arrow-like profile at the leading edge of the accretion. Accretion "b" was still devoid of feather like features and the small ridge near the stagnation line persisted. Accretion "c" had more growth normal to the chord with feather-like features along the top and bottom portions of the accretion aft of the leading edge. Unfortunately, accretion "d" was an early test point and was stopped after 180 seconds of cloud exposure. Accretion "e" in Figure 16 formed a double-horn structure after 600 seconds and had very fine feather-like features. Accretion "e" continued to be located on the center hollow-portion of the model whereas accretions "b" and "c" extended well onto the solid airfoil extensions. Small insets of the overall ice accretion for accretion "c" and "e" were added to Figure 16 – these images are from just after spray termination when the top-view camera was zoomed out to see the overall extent of the ice shape.

Figure 17A shows the leading edge growth rate, m, measurements for accretions "b" – "e". The listed values of m in the figure are the slopes from linear curve fits of the data between 120-180 seconds and 540-600 seconds, where data is available. Accretions "b","c", and "d" all had similar growth rates in the early period ($m = 0.24$-0.26 mm/s) although each accretion took longer to begin steady growth. Accretion "b" began steady growth almost immediately after spray initiation while accretions "c" and "d" took approximately 30 and 56 seconds, respectively, before beginning growth. Accretion "e" took in excess of 300 seconds before steady growth began. Towards the end of the accretion test, the growth rate slowed slightly for accretions "a" to 0.21 mm/s while accretion "b" and "d" increased to 0.39 mm/s.

The bottom four graphs of Figure 17 show the surface temperature measurements for the accretions "b" through "e". Just prior to spray initiation, each thermocouple (TC) measured ~6 ± 0.5°C. In all cases, the leading edge thermocouple (TC03) reached ~ 0°C within a few seconds of spray activation. With the exception of accretion "b", TC03 remained at ~ 0°C for the duration of the test. After about 60 seconds during accretion "b", TC03 began slowly decreasing and continued to do so for the remainder of the test reaching -3.6°C after 600 seconds. The remaining TCs for accretion "b" all eventually measured well below 0°C with the coldest reaching -5.6°C. In accretion "b", only TC03 and TC06 were covered with the ice accretion. Accretion "c" similarly had all thermocouples aft of the leading edge eventually reach below zero except the colder temperature only reached about -3.0°C. Accretion "d" was only a 180-second test but had similar trends to accretions "b" and "c". Finally, the surface temperature time history for accretion "e" was markedly different with the others cases in Figure 17. Here the thermocouples all reached about 0°C with TC14 taking over 180 seconds to reach that temperature. The temperature behavior of accretion "e" was similar to accretion "a" from Figure 14 and also had a similar resembling accretion.

Figures 18 and 19 show data from accretion "f" which was the only case tested with the airfoil from the 135 m/s, 15 μm MVD_i tests. After 180 seconds, the side view profile shows a double-horn shape ice accretion beginning to form. By 600 seconds, the double-horn shape is very pronounced. During this test, the backlight failed but the ice structure was still visible with the available lighting. Small feather-like features are visible in both the side and top-view images. The ice extends well onto the solid portion of the airfoil.

Figure 19A shows the ice thickness at the model centerline. Between 120-180 seconds, the growth rate is 0.64 mm/s. This test had a small partial shed of ice near midspan around 420 seconds losing a few millimeters of ice thickness locally. However, the ice quickly regrew in that area. Between 540 and 600 seconds, the growth rate slowed to 0.33 mm/s. Figure 19B shows the surface temperature measurements for this test. The leading edge thermocouple (TC03), rapidly cooled to 0°C and remained at this temperature for the entire test. With the exception of TC06, the remaining thermocouples all measured temperatures below 0°C with a slight continuous cooling trend. The coldest temperature measurements were from TC10 and TC13 which reached about -2.5°C. TC06 initially had a cooling trend but then warmed abruptly just after 180 seconds. Examination of the video data suggests nothing unusual happened around this time. In fact, the video showed that TC06 was covered by a thin ice layer within after approximately 30 seconds after spray initiation.

Figures 20 through 23 show data from ice accretions "g" and "h" which occurred at the higher speed of $v_T = 135$ m/s and larger MVD_i of 50 μm with plenum relative humidity values of ~10% and 25%, respectively, Both of these ice accretions formed larger leading-edge thickness on the solid airfoil extensions away from the model centerline. In fact, close examination of the images in Figures 20 and 22 show that there was no ice accreted on the leading edge of the model along the center hollow-portion. From the video, it appeared that that the ice on the model centerline began forming aft on the model and grew forward from an anchor point. Whereas the ice on the solid model extensions appeared to "anchor" further forward on the model resulting in larger leading edge thickness further away from the model center. Where it accreted away the centerline, ice accretion "g" had a more convex leading edge while accretion "h" had a concave leading edge appearance. Since no ice accreted at the midspan leading edge, no ice thickness measurements are presented.

Figure 21 (accretion "g") shows that both TC03 and TC06 both measured 0°C shortly after spray initiation and remained at this temperature for the duration of the test. The remaining thermocouples measured temperatures below freezing with the coldest measurements reading almost -6.0°C (TC13 and 14). Figure 23 (accretion "h") showed similar behavior although in this case TC03,TC06, and TC07 all measured 0°C shortly after spray initiation and remained at this value for the duration of the test. In addition, the coldest temperature measured for this case was about -2.7°C (TC13 and 14).

IV. Discussion

The overarching goal of tests like that described in this paper is to improve understanding of the physics of ice-crystal icing. The present research seeks to generate a prescribed mixed-phase condition at the duct exit plane of PSL similar to what occurs in an engine during ice crystal icing. In an engine, the mixed-phase environment is created by shattered ice particles that partially melt in the warmer-than-freezing environment of the engine. For the present tests at PSL, the mixed-phase cloud in an otherwise warmer-than-freezing environment is generated by partially freezing an initially liquid cloud using evaporative cooling. Regardless of whether or not the partial freeze out method

sufficiently mimics engine icing, the dataset gathered in these experiments will help develop ice-crystal (i.e. mixed-phase) icing models as well as further develop technology to measure the mixed-phase conditions.

For the above-freezing conditions presented in this paper ($T_{0,T}$ = 7.2°C, $P_{0,T}$ = 44.8 kPa, v_T = 85 and 135 m/s), a range of mixed-phase conditions was achieved by varying the plenum relative humidity. Complete cloud freezeout occurred only for the smaller particles size cloud (MVD_i = 15 μm) at both tested speeds. However, there was still liquid present with the larger particle size cloud (MVD_i = 50 um) even with a 0% plenum relative humidity. To achieve, freezeout in these cases, the temperature or pressure need to be reduced further. Fully liquid clouds were archived for the conditions tested when the plenum relative humidity was sufficiently high (~50 to 60%).

The wet-bulb temperature gauges whether the particles will supercool and / or freeze with smaller droplets cooling more quickly than larger droplets. Due to the flow acceleration, the static temperature (hence the static wet-bulb temperature) decreases as the flow passes through the PSL contraction to the duct exit plane. In the present experiments, the static temperature drop for the 85 m/s cases was still above freezing and evaporative cooling was required to freeze water droplets. For the 135 m/s cases, the static temperature drops below freezing but residence times in the cold contracted region are quite short and evaporative cooling was still required to achieve some freezing. The actual amount of freezing achieved (i.e. melt ratio) for a given test is a complex function of the parameters such as particle size, flow speeds, air temperature, water temperature, pressure, and humidity. An analytical model is being developed to predict the melt ratio (and other PSL parameters) with data presented in this paper used to help develop and validate such models. A complementary paper[20] is presented at this conference which compares model predictions to measurements from this experiment.

The melt ratios presented in this paper were estimated from the adjusted LWC measurements from the SEA multi-wire probe and the TWC measurements using the IKP2. The two LWC measurements provided by the multiwire probe come from different cylindrical elements (i.e. hot wires) which have different sensitivities to ice and water. In the present work, the values from the larger 2.1-mm diameter wire was used since it typically measured higher values of LWC. The measured LWC was adjusted for collision efficiency estimates from previous work and on data from this experiment, for watch catch efficiency from liquid water and false response due to impinging ice crystals. These adjustments are based on very limited available data and are likely applicable only to the tested flow conditions. Furthermore, additional adjustments may be required in mixed-phase conditions.

The measured *TWC* under the different conditions tested requires further interpretation. For the data presented in this paper, the amount of water injected was such that a *TWC* of 2 g/m^3 would be achieved across a 61 cm (24") diameter area at the duct exit plane. Such a *TWC* would be realized if no water evaporated and the particles were uniformly distributed across this area. However, water evaporation does occur and a non-uniform distribution of the water particles exists. Furthermore, the initial nozzle pattern was limited to the centermost nozzles – the desire being to keep all water in the center part of the tunnel so that it would be visible to the tomography system. Using the projected area of the initial nozzle pattern (adjusted for some expansion of the nozzle plume) onto the duct exit plane, the calculated *TWC* assuming no evaporation and uniform distribution was about 6.5 g/m$^{3.}$ This higher *TWC* is more consistent with the locally measured TWC_m using the IKP2 at the tunnel centerline which measured as high as 8 g/m^3. However, there were measured values as low as 1 g/m^3, presumably due to significant evaporation. While there is good confidence in the centerline IKP2 measurement of *TWC* (hence the data is useful for accretion modelling), additional work is required to understand why the *TWC* varies as it does across the conditions of this test

The non-uniformity of the cloud also required adjustments to the cloud-on humidity and temperature measurements which were measured approximately 24.5 cm (9.65") from the tunnel centerline. During the first day of testing, traverse measurements of the cloud radial profile were made which showed larger changes in temperature and humidity at the tunnel centerline compared with the periphery of the cloud. Based on those results, the temperature and humidity measurements were adjusted to approximate the centerline values. Although they are likely better representations of the conditions at the tunnel centerline (i.e. the primary location for ice accretion), the adjusted values are not direct measurements and thus increase the uncertainty. Future tests will attempt to make all temperature and humidity measurements at the tunnel centerline.

The ice accretions observed in the presented tests ranged from sharp arrow-like accretions, characteristic of ice-crystals causing some erosion, to cases with double-horn shapes, characteristic of supercooled water accretions. The accretions characteristic of erosion occurred at lower melt ratios while the double-horn case occurred at a higher melt ratios. As the water droplets freeze, they likely transition through a supercooled state. By the time they reach the test section at PSL, the smallest droplets freeze first with the larger droplets taking longer. Thus, the clouds generated during the present tests likely contain a mixture of smaller ice particles with large droplets of supercooled water. This is different than what occurs in an engine where the smallest particles melt first with larger particles remaining frozen.

Further work is required to verify the state and temperature of the droplets at the PSL test section. In addition, the ice accretions generated with partially frozen clouds need to be compared to ice accretions generated with partially melted clouds. Nonetheless, the presented results offer a valuable dataset to modelers of ice accretion.

V. Conclusions

NASA is investigating the fundamental physical mechanisms of icing that occurs in core compressor regions of jet engines when ingesting ice crystals. The overarching goal of these tests is to improve understanding of the ice growth physics and expand engine aero-thermodynamic modeling capability to predictively assess the onset of icing in current and future aircraft. Enablers for this modelling capability are fundamental experiments to understand ice-crystal icing physics that determine the conditions favorable for ice accretion and the rate of ice growth. NASA seeks to develop capability to generate a prescribed mixed-phase condition similar to what occurs inside a jet engine when accreting ice. However, it is desired to generate that environment outside of an engine to facilitate study. NASA is examining PSL as a potential test-bed for such research. The data presented in this paper focuses on the conditions at the test section (PSL duct exit plane) namely (1) the freeze out characteristics of the cloud, (2) changes in aerothermal conditions due to the presence of the cloud, and (3) the ice accretion characteristics observed. The primary variable in this test was the plenum humidity which was systematically varied for two duct-exit-plane velocities (85 and 135 m/s) as well as two particle size clouds (15 and 50 µm MVD_i). The observed clouds ranged from fully glaciated to fully liquid, where the liquid clouds were at least partially supercooled. Significant radial variation of measured temperature and humidity necessitate adjustment of measurements in the cloud periphery to approximate tunnel centerline characteristics where the ice-growth was being measured. The ice accretions observed ranged from sharp arrow-like accretions, characteristic of ice-crystals causing some erosion, to cases with double-horn shapes, characteristic of supercooled water accretions. The presented results offer modelers a dataset to help develop ice accretion models.

Acknowledgment

The authors wish to acknowledge the financial support for this work by the Advanced Aircraft Icing (AAI) Subproject of the NASA Advance Air Transport Technology Project (AATT) under NASA's, Advanced Air Vehicle's program.

References

[1]Mason, J. G., Strapp, J. W., and Chow, P. "The Ice Particle Threat to Engines in Flight," *44th AIAA Aerospace Sciences Meeting and Exhibit*, AIAA-2006-206, 2006.

[2]Wright, W. B., Jorgenson, P. C. E., and Veres, J. P. "Mixed Phase Modeling in GlennICE with Application to Engine Icing," *AIAA Atmospheric and Space Environments Conference*, AIAA-2010-7674, AIAA 2010-7674, 2010.

[3]Currie, T. C., Fuleki, D., and Mahallati, A. "Experimental Studies of Mixed-Phase Sticking Efficiency for Ice Crystal Accretion in Jet Engines," *6th AIAA Atmospheric and Space Environments Conference*, AIAA-2014-3049, 2014.

[4]Villedieu, P., Trontin, P., and Chauvin, R. "Glaciated and mixed phase ice accretion modeling using ONERA 2D icing suite," *6th AIAA Atmospheric and Space Environments Conference*, AIAA-2014-2199, 2014.

[5]Wright, W., Struk, P., Bartkus, T. P., and Addy, G. "Recent Advances in the LEWICE Icing Model," *SAE 2015 International Conference on Icing of Aircraft, Engines, and Structures* SAE Technical Paper 2015-01-2094, 2015.

[6]Griffin, T. A., Lizanich, P., and Dicki, D. J. "PSL Icing Facility Upgrade Overview," *6th AIAA Atmospheric and Space Environments Conference*, AIAA-2014-2896, 2014.

[7]Oliver, M. J. "Validation Ice Crystal Icing Engine Test in the Propulsion Systems Laboratory at NASA Glenn Research Center," *6th AIAA Atmospheric and Space Environments Conference*, AIAA-2014-2898, 2014.

[8]Flegel, A. B., and Oliver, M. J. "Preliminary Results from a Heavily Instrumented Engine Ice Crystal Icing Test in a Ground Based Altitude Test Facility," *8th AIAA Atmospheric and Space Environments Conference, AIAA Aviation and Aeronautics Forum and Exposition 2016*, American Institute of Aeronautics and Astronautics, Washington, D.C. (submitted for publication).

[9]Struk, P. M., Tsao, J. C., and Bartkus, T. P. "Plans and Preliminary Results of Fundamental Studies of Ice Crystal Icing Physics in the NASA Propulsion Systems Laboratory," *8th AIAA Atmospheric and Space Environments Conference*, AIAA-2016-3738, 2016.

[10]Struk, P. M., Bartkus, T. P., Tsao, J. C., Currie, T., and Fuleki, D. "Ice Accretion Measurements on an Airfoil and Wedge in Mixed-Phase Conditions," *SAE 2015 International Conference on Icing of Aircraft, Engines, and Structures*, SAE Technical Paper 2015-01-2116, 2015.

[11]Bencic, T. J., Fagan, A. F., Van Zante, J. F., Kirkegaard, J. P., Rohler, D. P., Maniyedath, A., and Izen, S. H. "Advanced Optical Diagnostics for Ice Crystal Cloud Measurements in the NASA Glenn Propulsion Systems Laboratory," *5th AIAA Atmospheric and Space Environments Conference*, AIAA-2013-2678, 2013.

[12]Van Zante, J. F., Bencic, T. J., and Ratvasky, T. P. "NASA Glenn Propulsion Systems Lab Ice Crystal Cloud Characterization Update 2015," *8th AIAA Atmospheric and Space Environments Conference*, AIAA-2016-3897, 2016.

[13]Van Zante, J. F., Ide, R. F., Steen, L. E., and Acosta, W. J. "NASA Glenn Icing Resarch Tunnel: 2014 Cloud Calibration Procedure and Results," NASA/TM-2014-218392, 2014.

[14]Strapp, J. W., Lilie, L. E., Ratvasky, T. P., Davison, C. R., and Dumont, C. "Isokinetic TWC Evaporator Probe: Development of the IKP2 and Performance Testing for the HAIC-HIWC Darwin 2014 and Cayenne Field Campaigns," *8th AIAA Atmospheric and Space Environments Conference*, AIAA-2016-4059 and NASA TM-2016-219151, 2016.

[15]Steen, L. E., Ide, R. F., and Van Zante, J. F. "An Assessment of the Icing Blade and the SEA Multi-Element Sensor for Liquid Water Content Calibration of the NASA GRC Icing Research Tunnel," *8th AIAA Atmospheric and Space Environments Conference*, AIAA-2016-4051, 2016.

[16]Rigby, D. L., Struk, P. M., and Bidwell, C. S. "Simulation of fluid flow and collection efficiency for an SEA multi-element probe," *6th AIAA Atmospheric and Space Environments Conference*, AIAA-2014-2752, 2014.

[17]Lilie, L., Emery, E., Strapp, J. W., and Emery, J. "A Multiwire Hot-Wire Device for Measurment of Icing Severity, Total Water Content, Liquid Water Content, and Droplet Diameter " *43rd AIAA Aerospace Sciences Meeting and Exhibit*, AIAA-2005-859, 2005.

[18]King, M. C., Bachalo, W., and Kurek, A. "TBD, High Speed Imaging and Phase Dopplet Interfeometry Measurements Paper," *9th AIAA Atmospheric and Space Environments Conference*, American Institute of Aeronautics and Astronautics, Denver, CO (submitted for publication).

[19]Veres, J. P., Jorgenson, P. C. E., Wright, W. B., and Struk, P. M. "A Model to Assess the Risk of Ice Accretion due to Ice Crystal Ingestion in a Turbofan Engine and its Effects on Performance," *4th Atmospheric and Space Environments Conference*, AIAA 2012-3038, 2012.

[20]Bartkus, T. P., Struk, P. M., and Tsao, J.-C. "Comparisons of Mixed-Phase Icing Cloud Simulations with Experiments Conducted at the NASA Propulsion Systems Laboratory," *9th AIAA Atmospheric and Space Environments Conference*, American Institute of Aeronautcs and Astronautics, Denver, CO (submitted for publication).

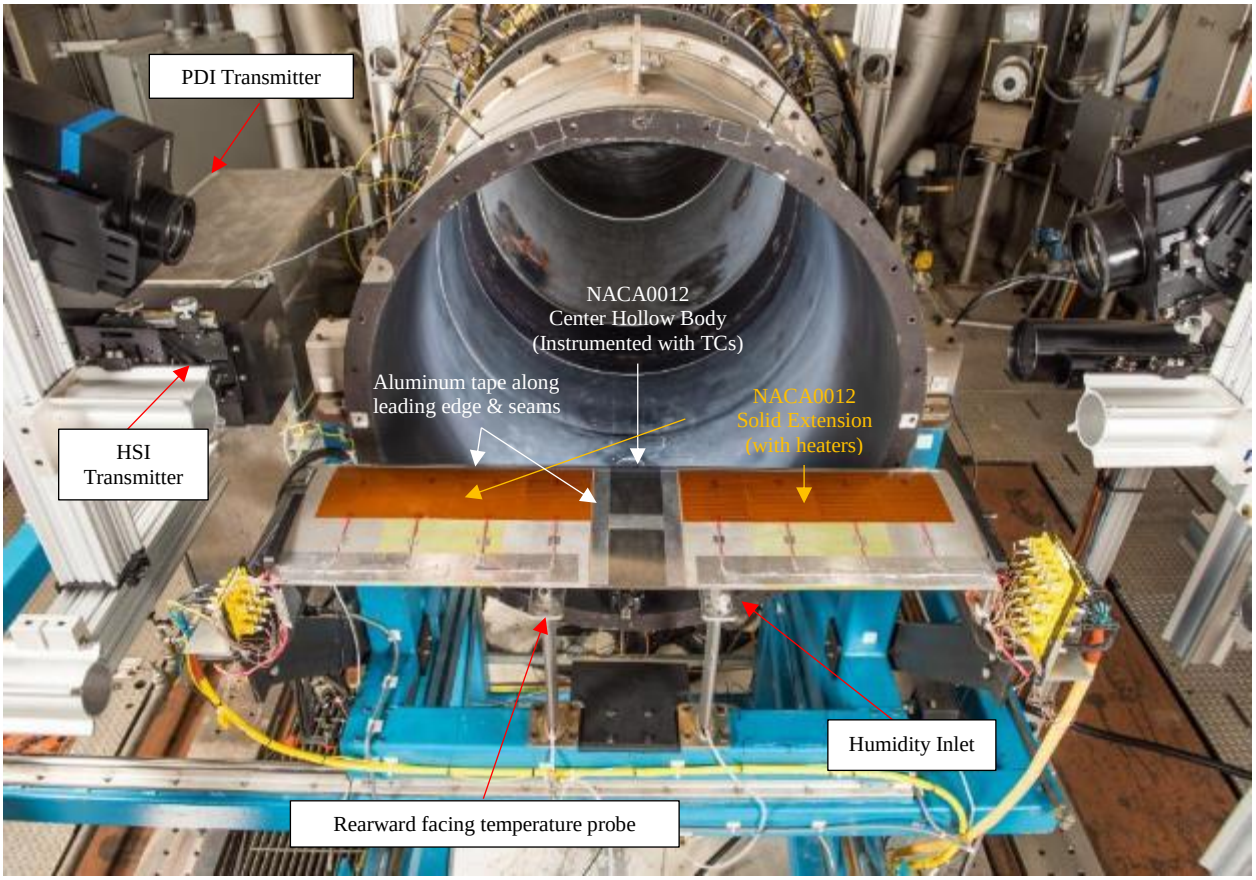

Figure 1. NACA0012 airfoil model placed at the exit of the PSL in a freejet configuration (test configuration 2)

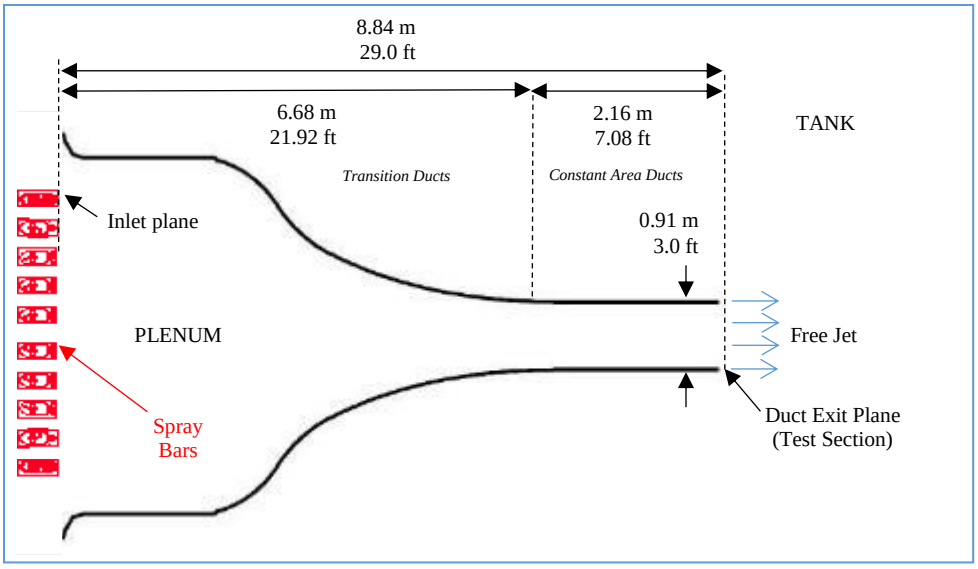

Figure 2. Schematic of PSL test configuration.

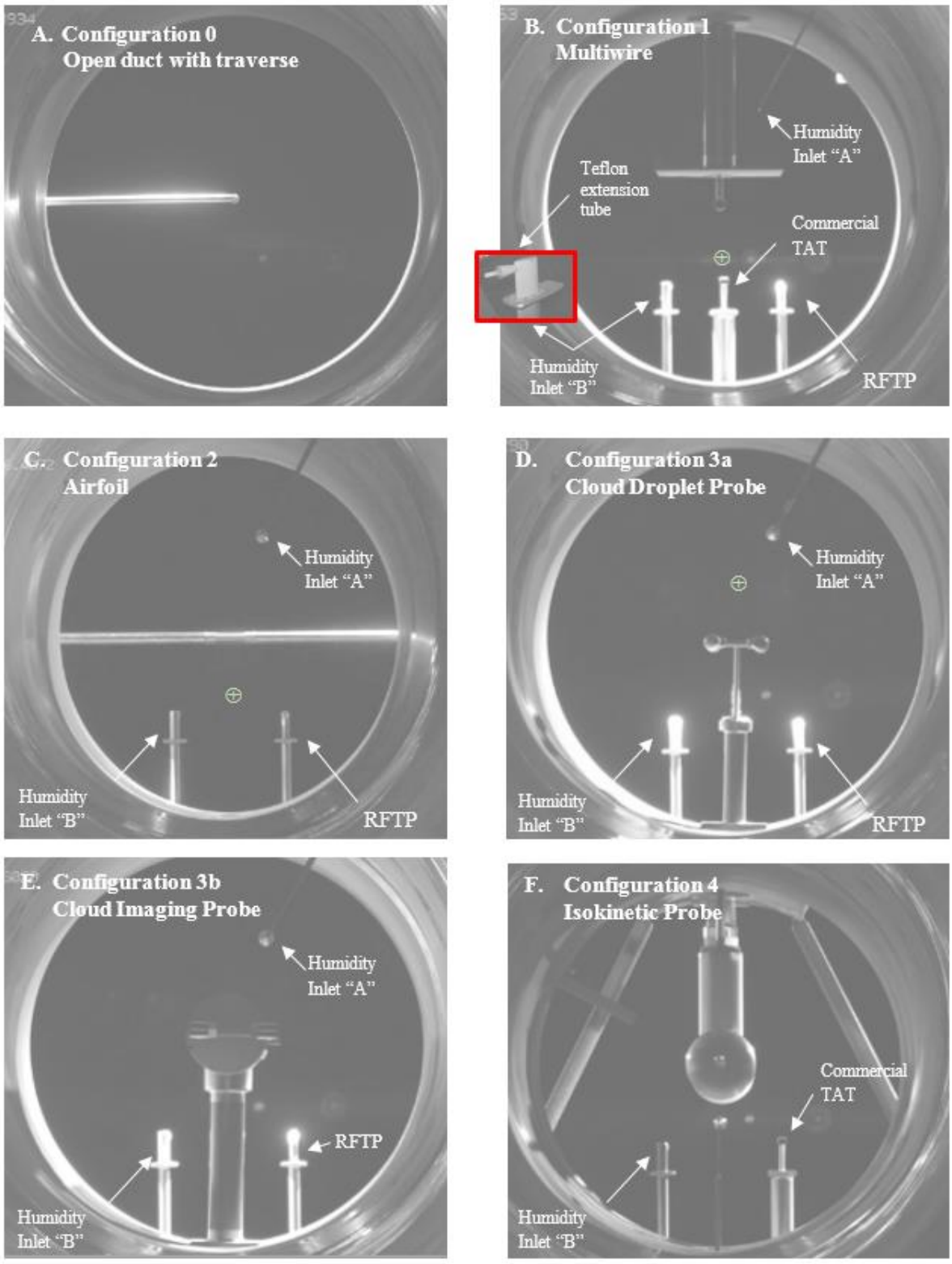

Figure 3. The various test configurations used during this test at the NASA Propulsion Systems Lab. The approximate location of the HSI and PDI sample volumes is shown with the symbol ⊕ in configurations 1, 2, and 3a.

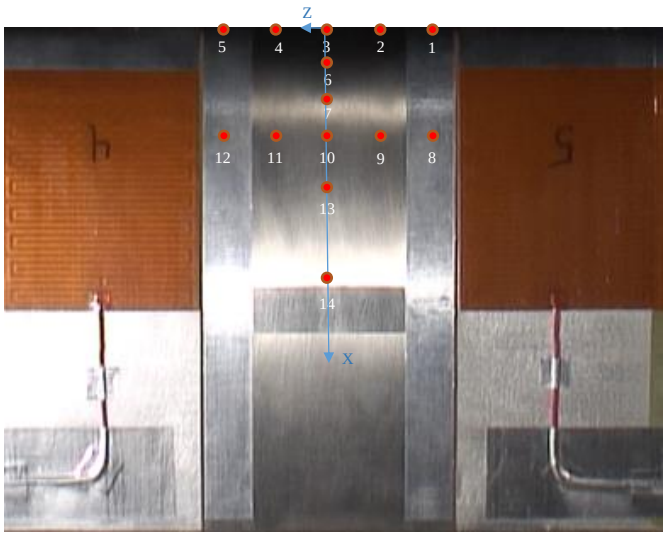

TC↓	X	Y	Z
1	0.000	0.000	-5.334
2	0.000	0.000	-2.667
3	**0.000**	**0.000**	**0.000**
4	0.000	0.000	2.667
5	0.000	0.000	5.334
6	**1.712**	**1.052**	**0.000**
7	**3.802**	**1.402**	**0.000**
8	5.918	1.560	-5.334
9	5.918	1.560	-2.667
10	**5.918**	**1.560**	**0.000**
11	5.918	1.560	2.667
12	5.918	1.560	5.334
13	**8.039**	**1.600**	**0.000**
14	**13.907**	**1.374**	**0.000**
15	13.907	0.000	0.000

Figure 4. Thermocouple locations definition – the units in the table are in centimeters. Coordinates are relative to the leading edge at midspan. The directions X and Z are as shown in the figure while the dimension Y is along the chord.

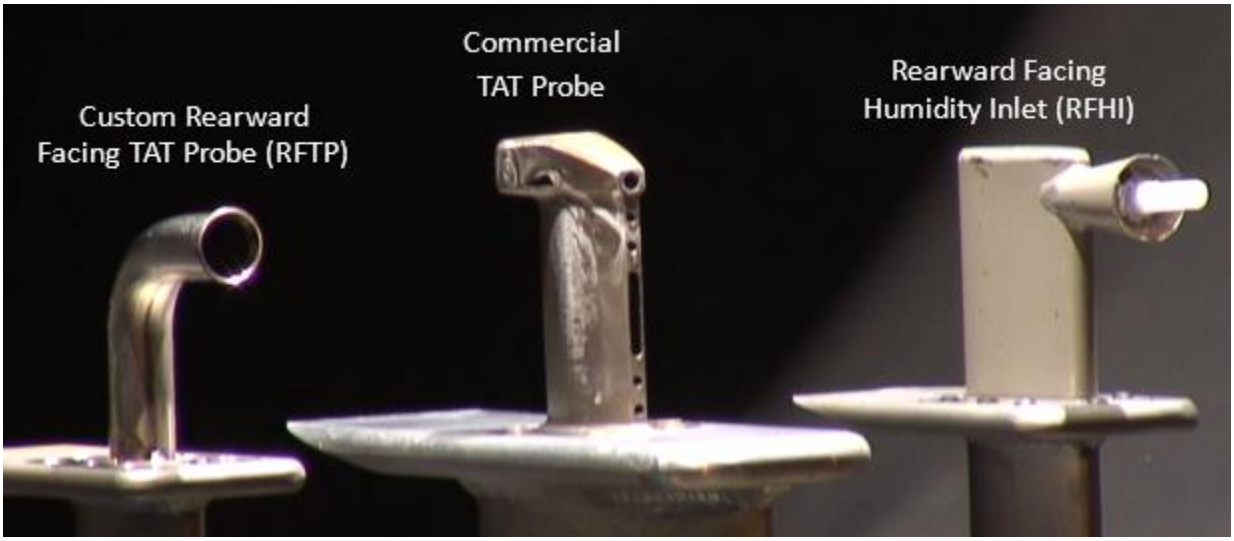

Figure 5. Temperature probes and humidity measurement inlet used during testing (shown in configuration 1).

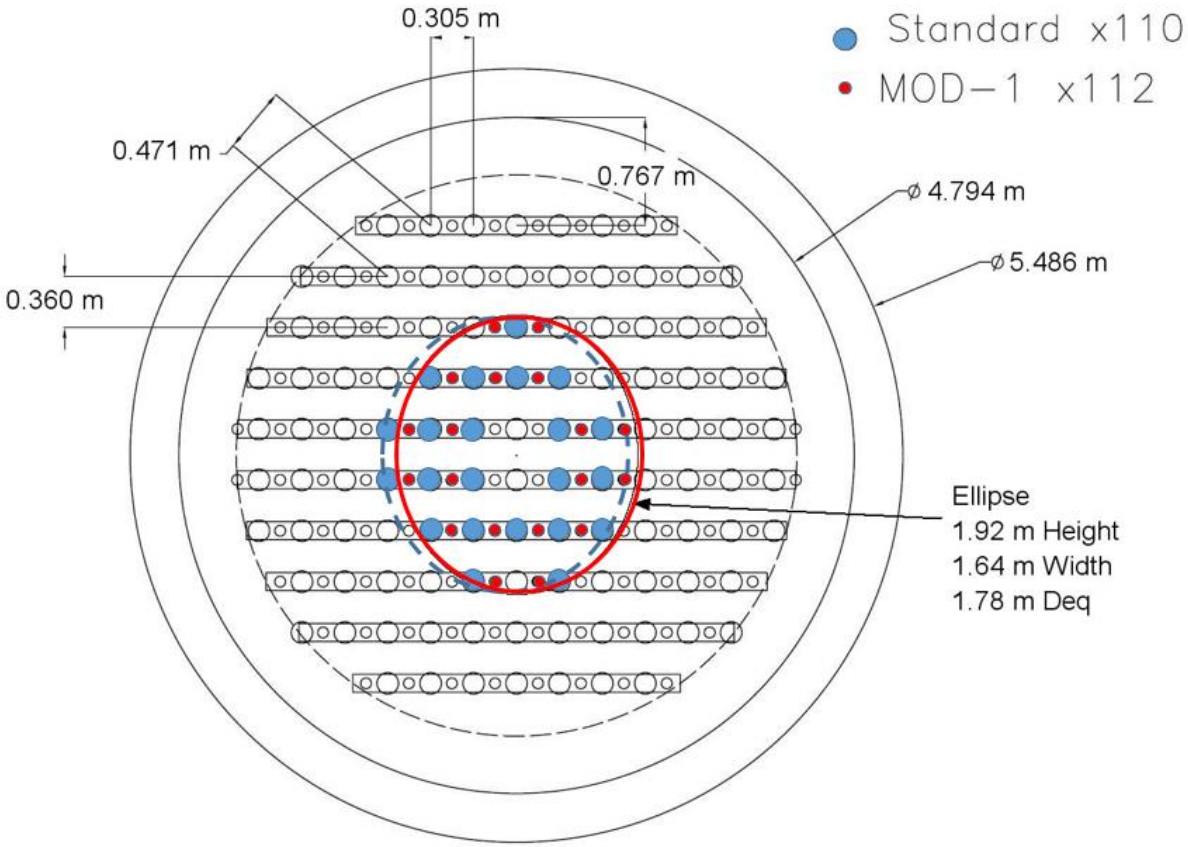

Figure 6. Nozzle patterns used during testing. The red circles denote the pattern for the Mod-1 nozzles (19 total) while the blue circles denote the pattern for the standard nozzles (22 total). The ellipse, colored to match the nozzle type, denotes the approximate initial coverage area of the spray. The larger OD of 5.486 m is the plenum diameter at the spray bars.

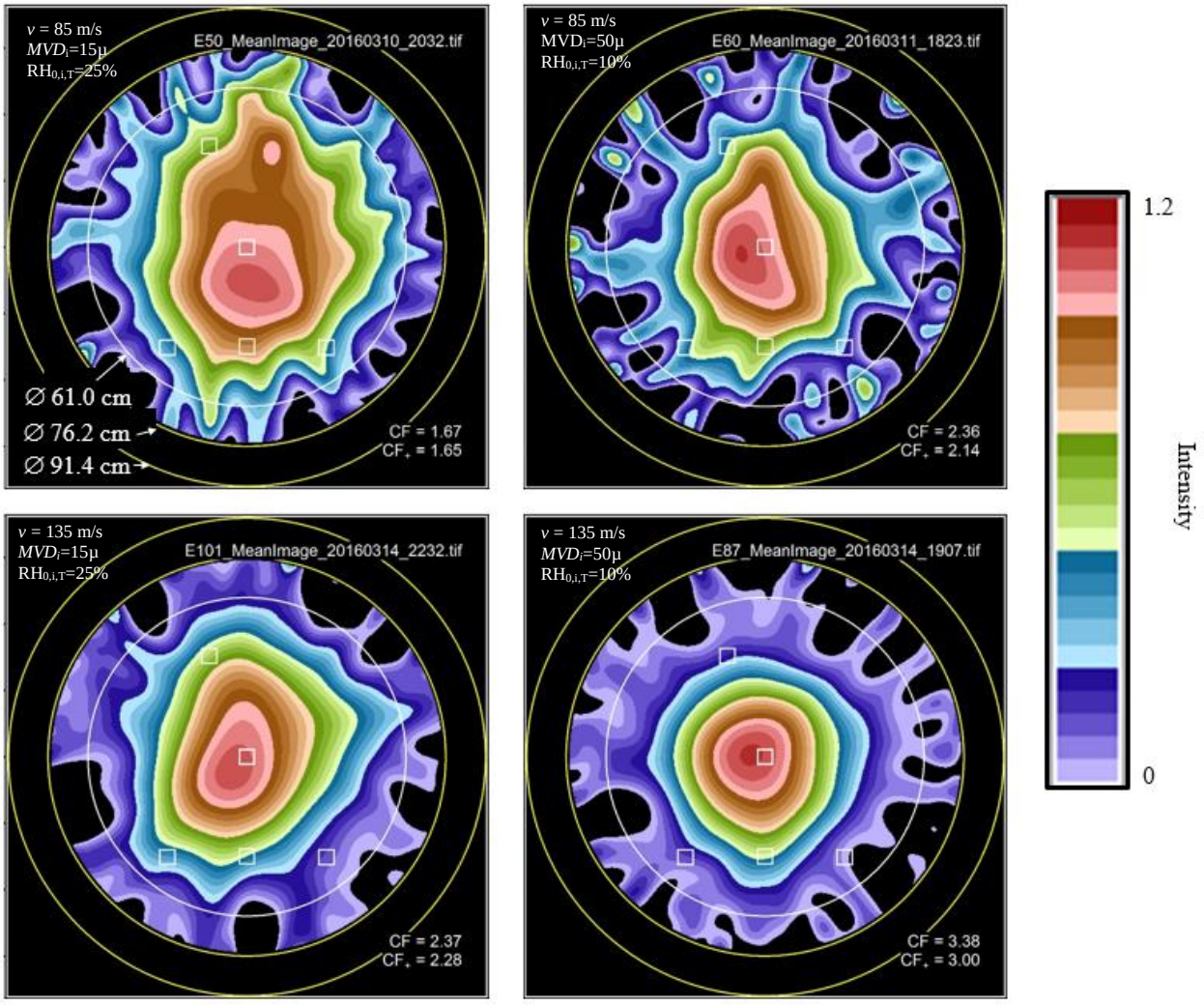

Figure 7. PSL tomography data showing four different tests from the plenum humidity sweeps (conditions shown in each figure). The concentration factors (CF) are the ratios of average intensity across the middle 2.54 cm x 2.54 cm (1" x 1") square area to the intensity across the 61.0 cm (24") diameter area. The ratio, CF+, uses only pixels with an intensity value greater than 0.01 while CF uses all pixels. The other square 1" regions overlaid in the image represent the locations of various probes during testing.

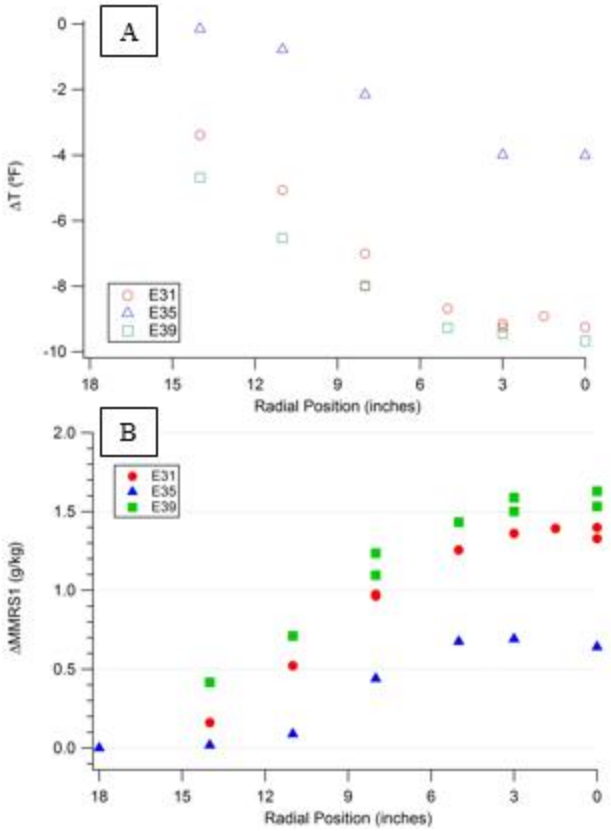

Test #	31	35	39
T_0 (°F)	50	50	50
P_0 (psia)	6.5	12.6	6.5
U (m/s)	85	135	85
TWC_i (g/m^3)	2	2	8.5
MVD_i (μm)	15	50	35

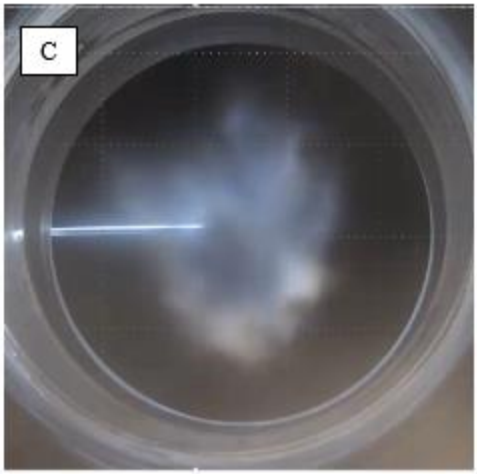

Figure 8. Radial temperature (A) and humidity (B) measurements taken during a traverse of the PSL cloud during configuration 0 of testing. The target conditions for each test are shown in the table. An image (C) from test 39 is inset in the figure showing the rearward facing inlet inserted almost to the tunnel centerline. For these tests, only a subset of the innermost spray bar nozzles were used to keep the cloud from impinging on the walls of the duct so that all water would be visible to the tomography system which is not sensitive to water near the duct wall. CHANGE TO CELCIUS.

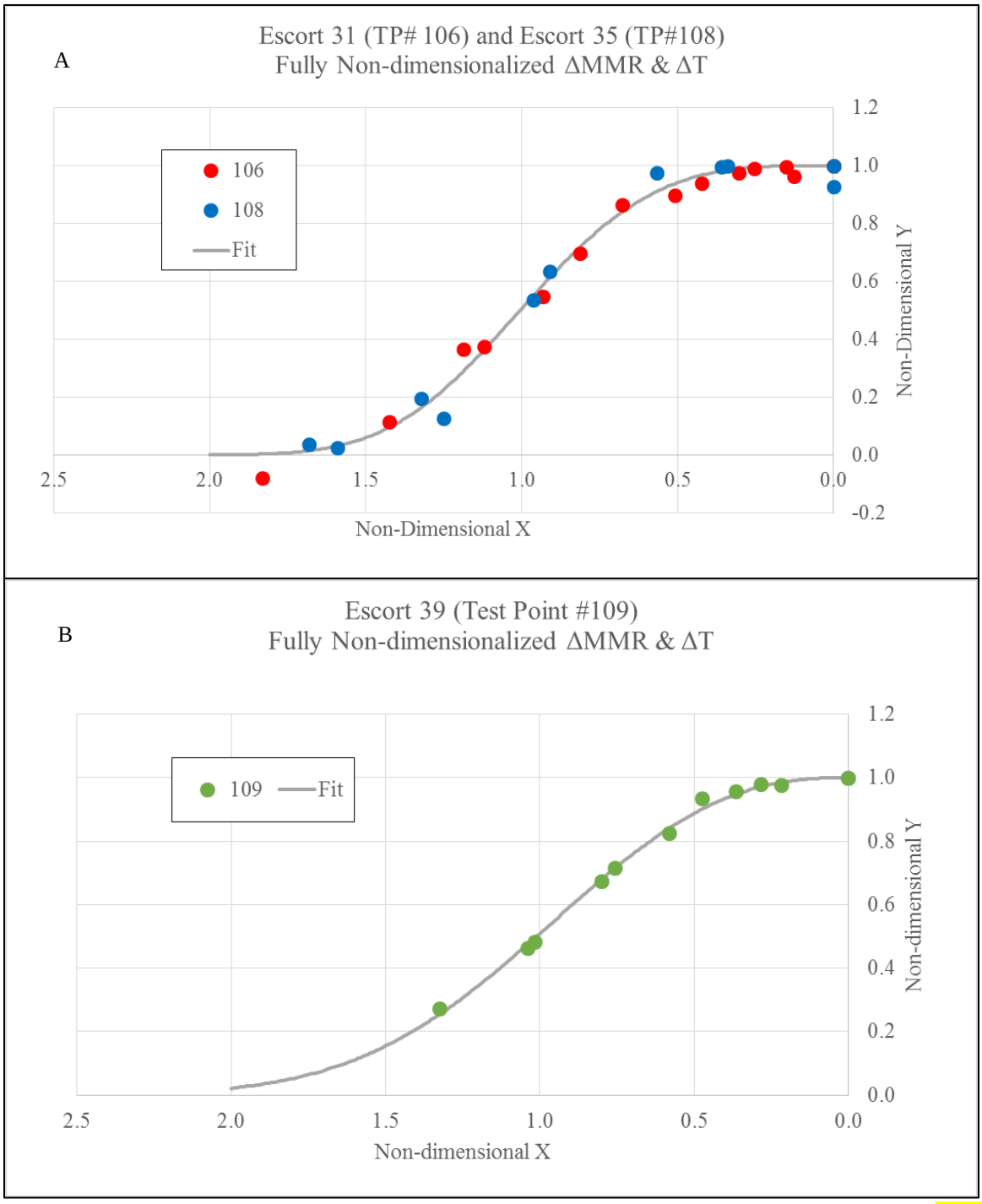

Figure 9. Non-dimensional profiles of # 106 and 108 (graph A) as well as # 109 (graph B) along with the curve fit. Maybe superimpose onto one figure.

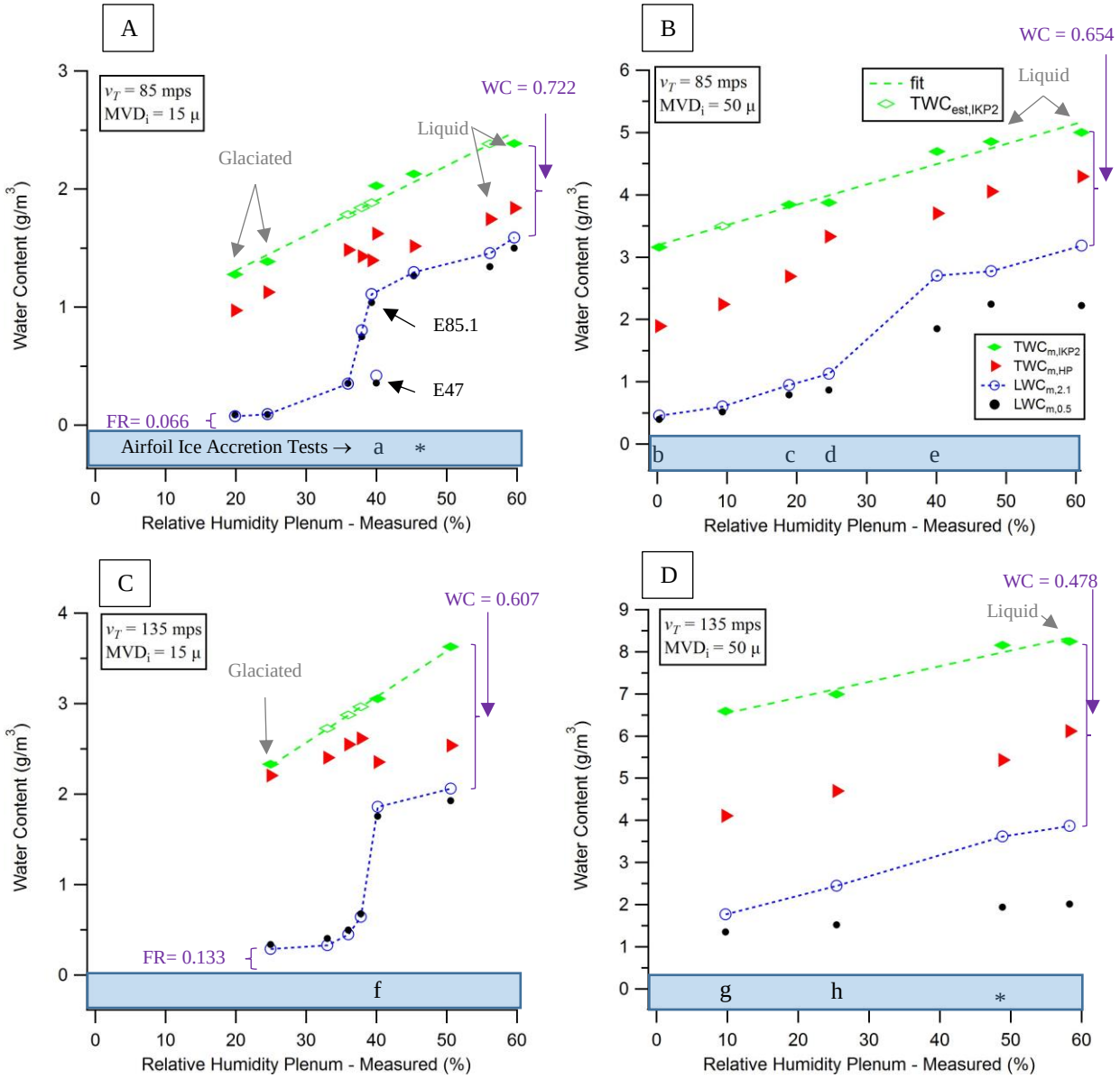

Figure 10. Water content measurements from 4 plenum humidity sweeps. The target velocity and initial particle size distribution, MVDi, are shown in each graph. The target facility conditions were P0,i,T = 44.8 kPa (6.5 psia) and T0,i,T = 7.2°C with a static pressure of 42.8 kPa (6.21 psia) and 40.0 kPa (5.8 psia) for the 85 and 135 m/s cases, respectively. Cloud which were observed to be fully glaciated or fully liquid are denoted in the figure – these observation were based on whether ice was observed to accrete on the probe in the tunnel. Conditions which were tested with the airfoil and produced ice accretion are denoted by letters in the blue box at the bottom of each graph. Asterisks (*) denote conditions tested with the airfoil that did not produce ice accretion. Finally, the figure shows the value used for false response (FR) and water catch (WC) efficiency in the melt ratio estimate.

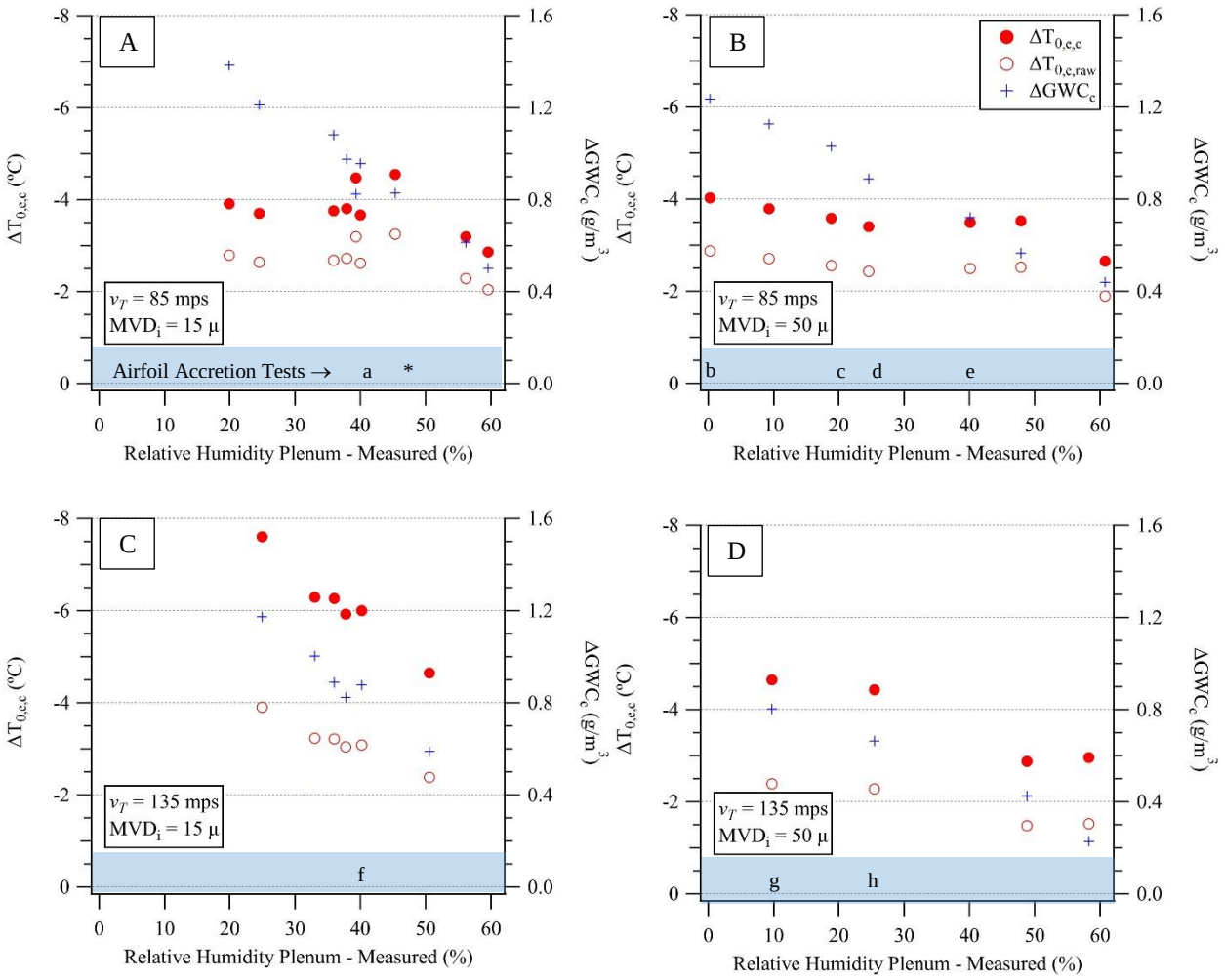

Figure 11. Changes in air temperature and air water content from 4 plenum humidity sweeps. The target velocity and initial particle size distribution, MVD_i, are shown in each graph. The target facility conditions were $P_{0,i,T}$ = 44.5 kPa (6.5 psia) and $T_{0,i,T}$ = 7.2 ℃ with a static pressure of 42.8 kPa (6.2 psia) and 40.0 kPa (5.8 psia) for the 85 and 135 m/s cases, respectively.

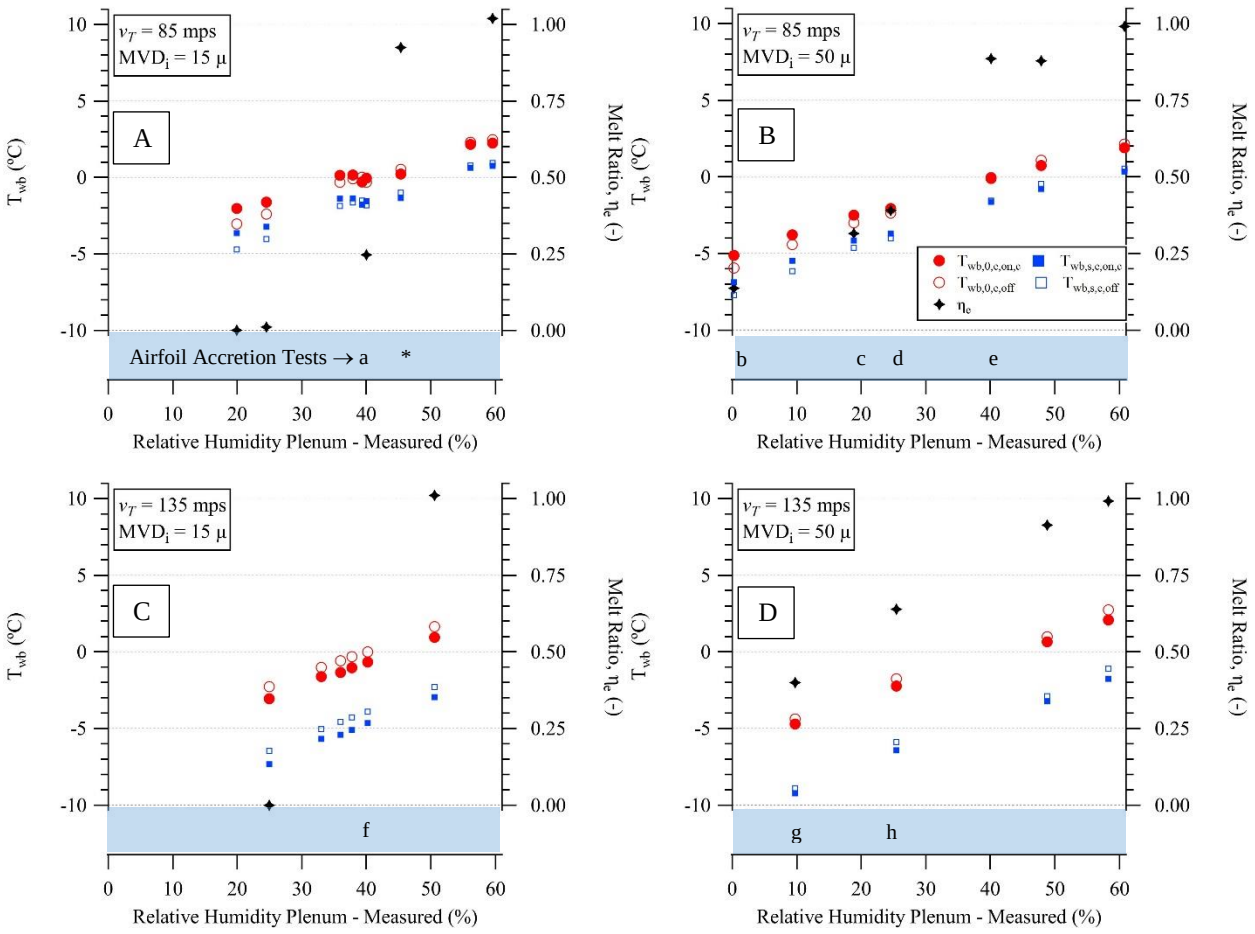

Figure 12. Wet bulb temperatures and estimated melt ratios at the plenum and duct exit plane as a function of plenum relative humidity. The target facility conditions were $P_{0,i,T}$ = 44.8 kPa (6.5 psia) and $T_{0,i,T}$ = 7.2 ℃ with a static pressure of 42.8 kPa (6.2 psia) and 40.0 kPa (5.8 psia) for the 85 and 135 m/s cases, respectively.

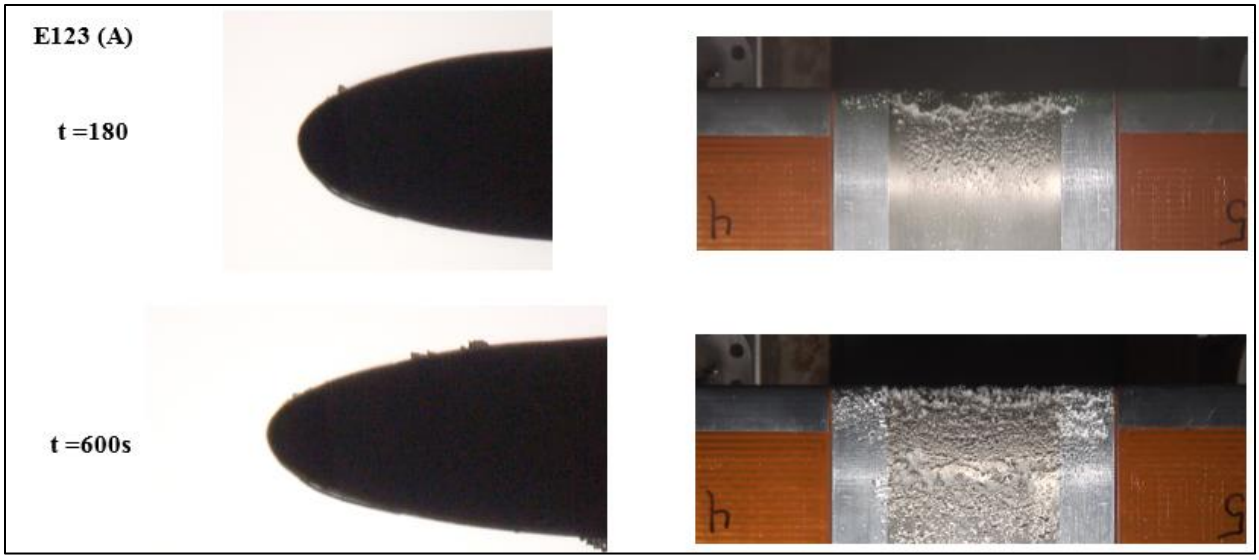

Figure 13. ***Ice Accretion "a"****: images taken after 180 seconds (top row) and 600 seconds (bottom row) of cloud exposure for a plenum relative humidity of ~40 % at 85 m/s and* MVD_i*=15 μ. The left column shows the side view profile and the right column shows a view from above the airfoil. The target aerothermal conditions were* $P_{0,i,T}$*=44.8 kPa (6.5 psia) and* $T_{0,i,T}$ *= 7.2 ℃ with a static pressure of 42.8 kPa (6.2 psia).*

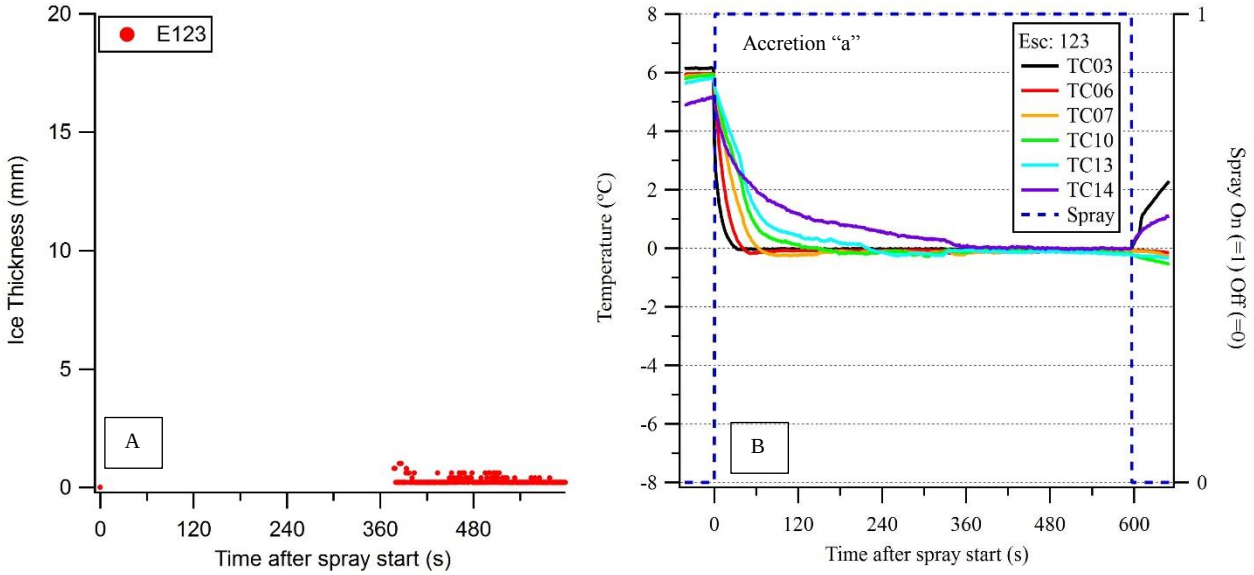

Figure 14. Ice thickness measurements versus time (graph A) and thermocouple measurements along airfoil centerline (graph B) for the ice accretion case "a" corresponding to v_T *= 85 m/s and 15μm* MVD_i*. The ice thickness measurements are made at the midspan of the model from the top-view images. The thermocouples locations are defined in Figure 4.*

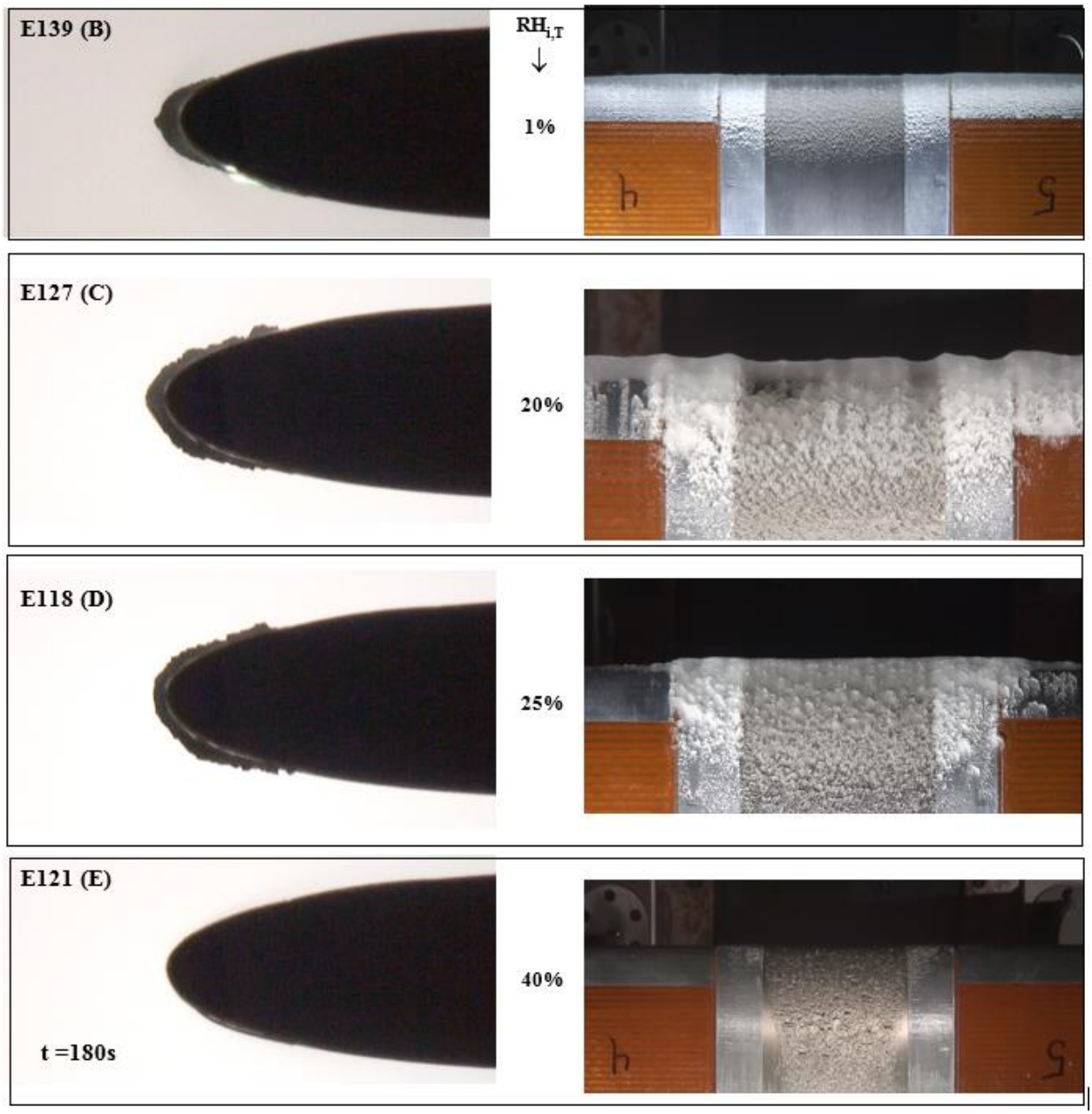

Figure 15. ***Ice Accretions "b"-"e"****: Images shown after 180 seconds of cloud exposure for 4 different plenum humidity values at 85 m/s and MVD$_i$=50 μ. The left column shows the side view profile and the right column shows a view from above the airfoil. The target aerothermal conditions were $P_{0,i,T}$ = 44.8 kPa (6.5 psia) and $T_{0,i,T}$ = 7.2 ℃ with a static pressure of 42.8 kPa (6.2 psia).*

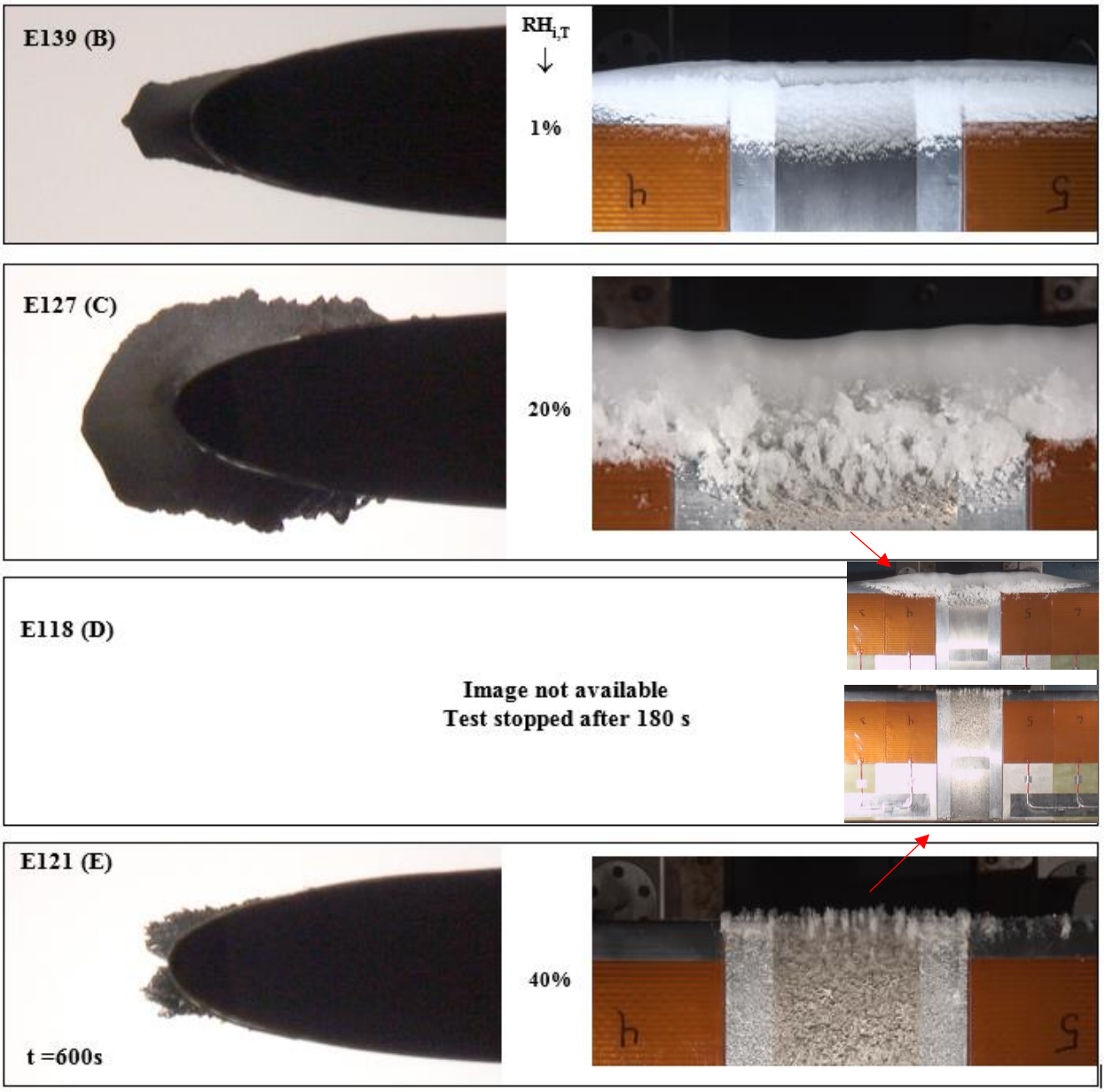

Figure 16. ***Ice Accretions "b"-"e":*** *images after 600 seconds of cloud exposure for 4 conditions shown in Figure 15.*

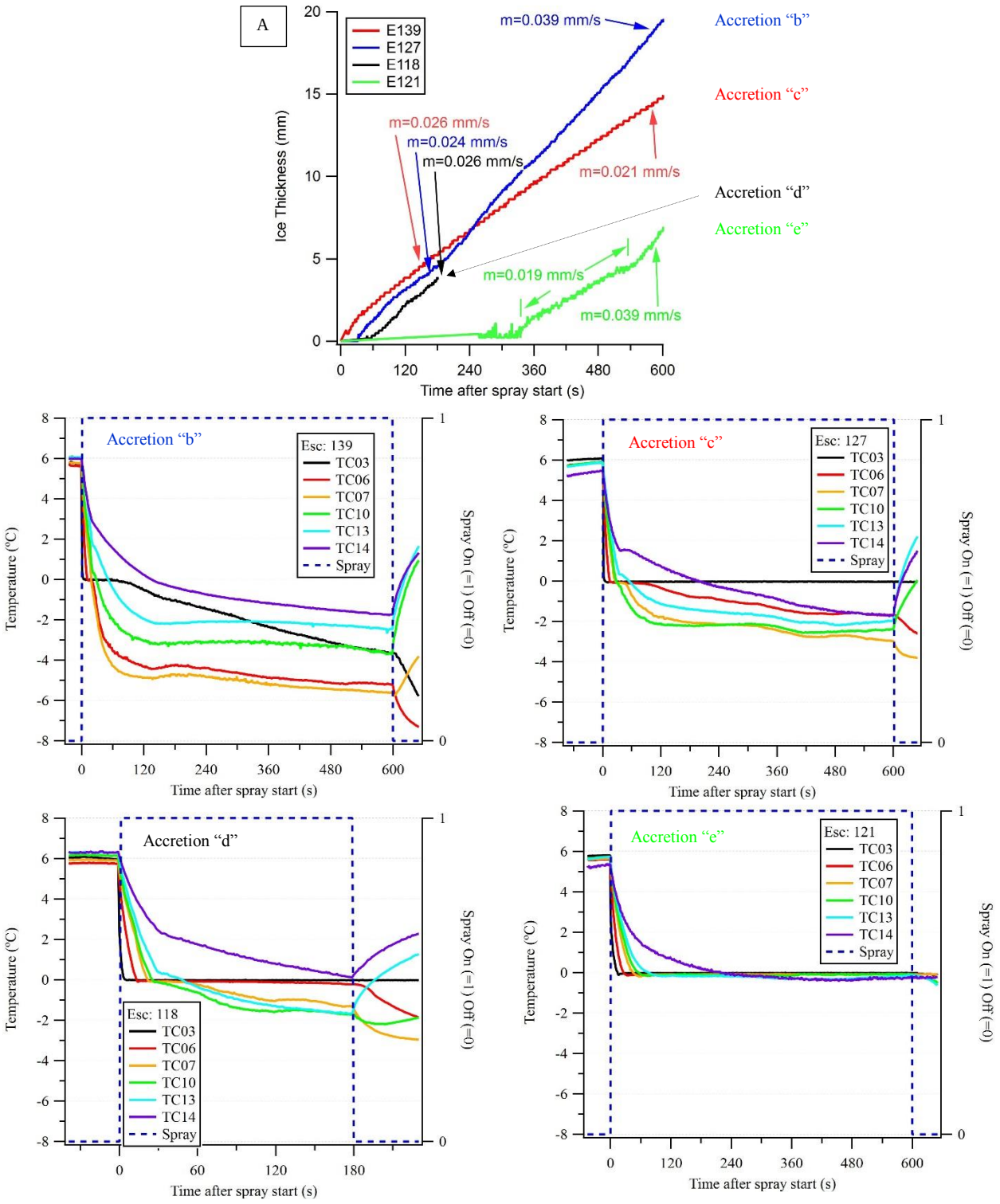

Figure 17. Ice thickness measurements versus time (graph A) and thermocouple measurements along airfoil centerline for the ice accretion cases "b" through "d" corresponding to v_T = 85 m/s and 50 μm MVD_i.

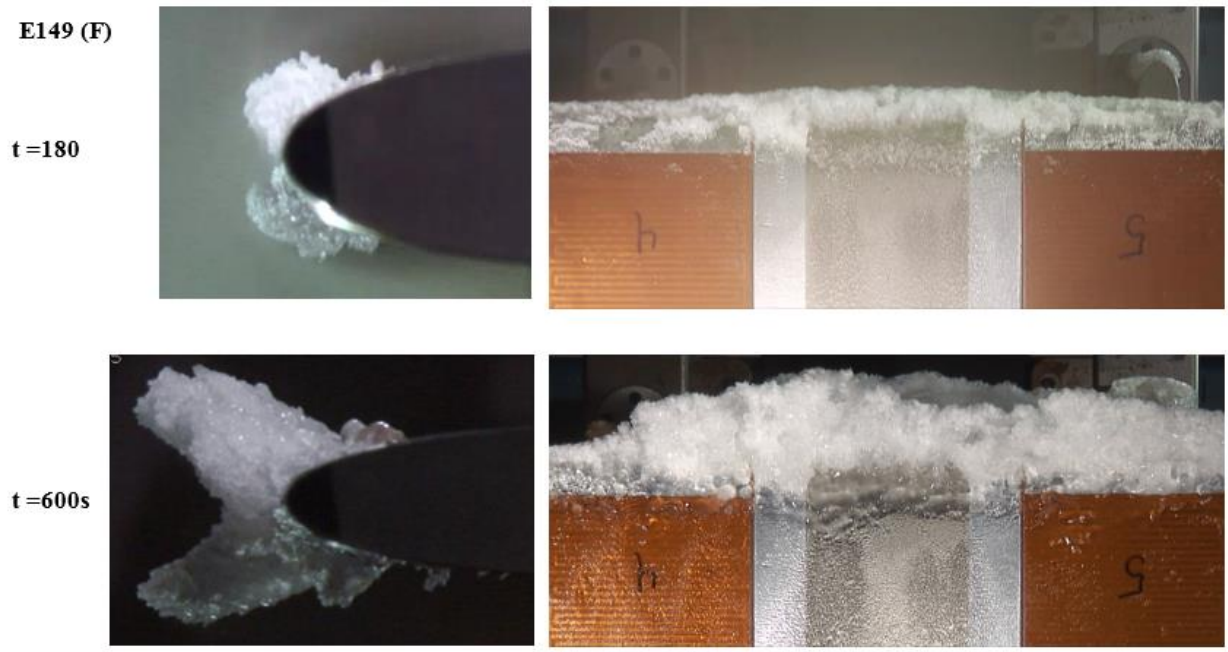

Figure 18. ***Ice Accretion "f":*** *Images after 180 seconds (top row) and 600 seconds (bottom row) of cloud exposure for a plenum relative humidity of ~40% at 135 m/s and MVD_i=15 μ. The left column shows the side view profile and the right column shows a view from above the airfoil. The target aerothermal conditions were $P_{0,i,T}$ = 44.8 kPa (6.5 psia)and $T_{0,i,T}$ = 7.2 ℃ with a static pressure of 40.0 kPa (5.8 psia).*

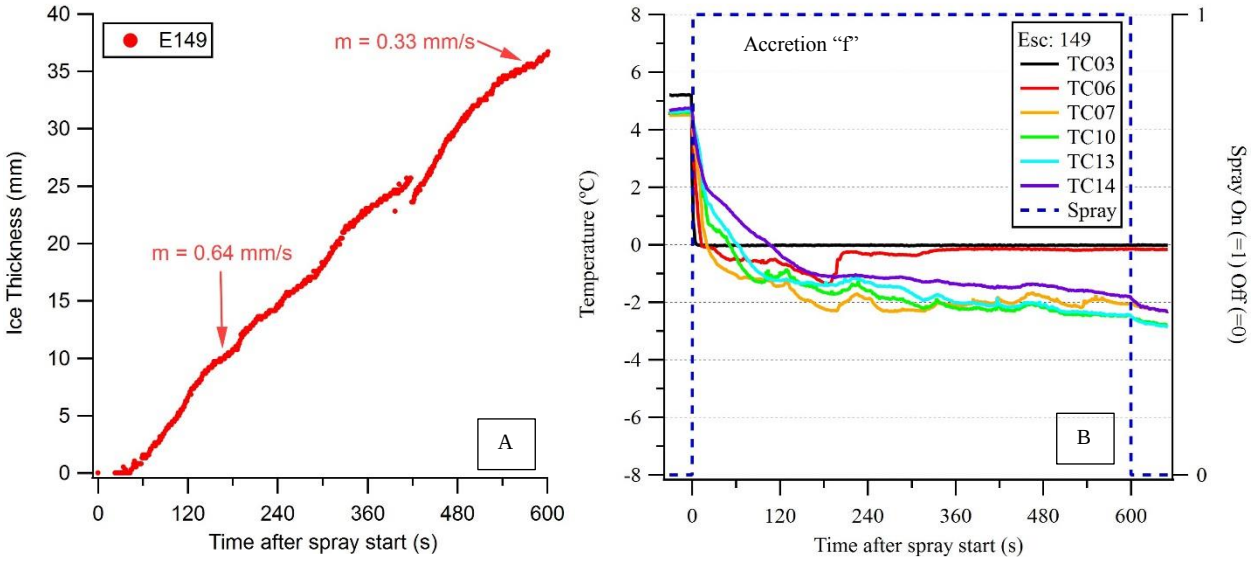

Figure 19. Ice thickness measurements versus time (graph A) and thermocouple measurements along airfoil centerline (graph B) for the ice accretion case "f". The ice thickness measurements are made at the midspan of the model from the top-view images. The thermocouples locations are defined in Figure 4.

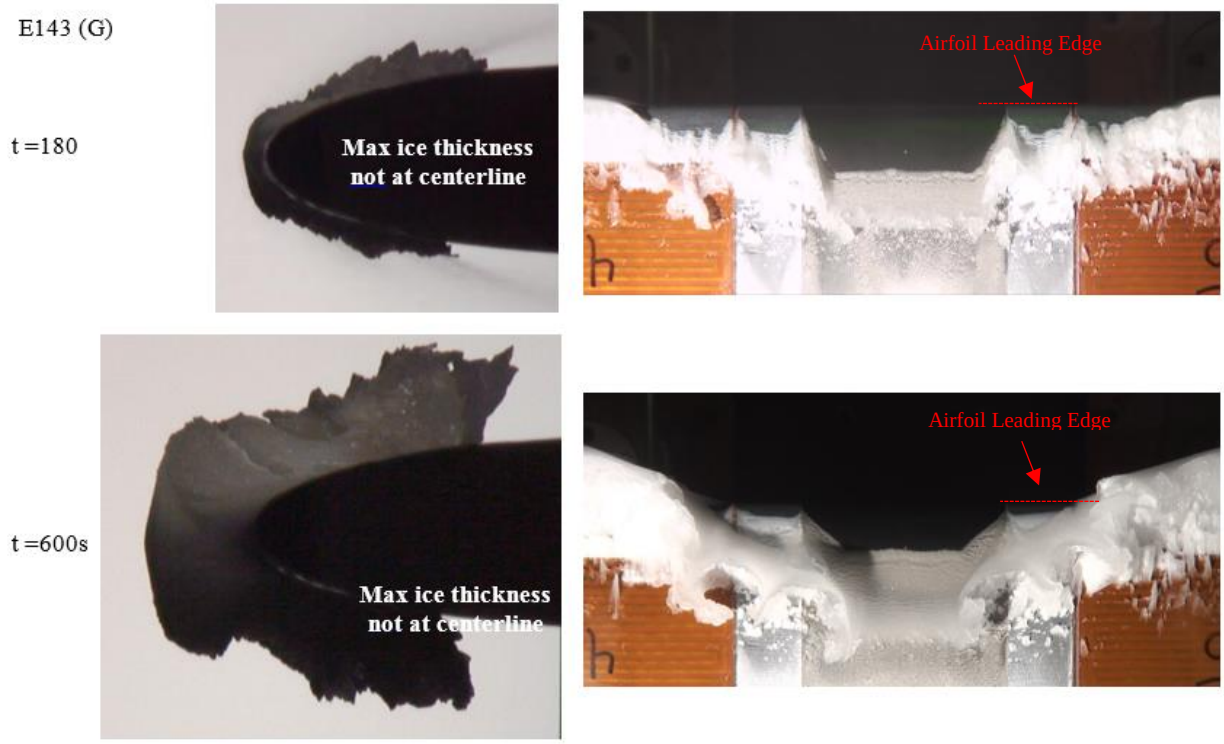

Figure 20. ***Ice Accretion "g":*** *Images after 180 seconds (top row) and 600 seconds (bottom row) of cloud exposure for a plenum relative humidity of ~10 % at 135 m/s and MVD_i=50 μ. The left column shows the side view profile and the right column shows a view from above the airfoil. The target aerothermal conditions were $P_{0,i,T}$ = 44.8 kPa (6.5 psia) and $T_{0,i,T}$ = 7.2 ℃ with a static pressure of 40.0 kPa (5.8 psia).*

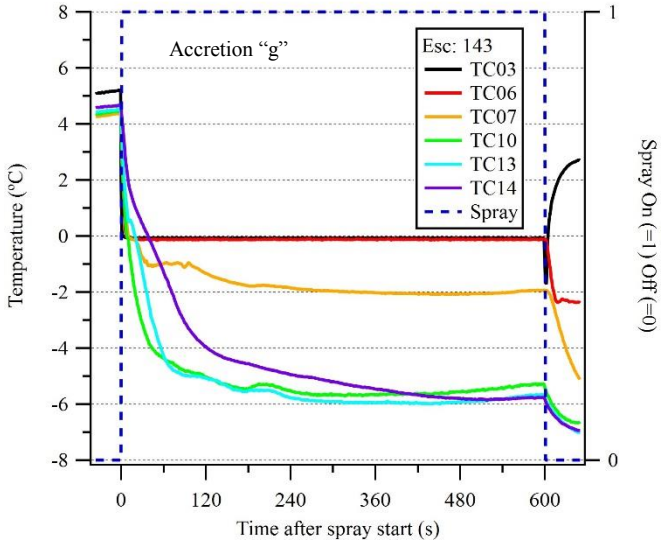

Figure 21. Thermocouple measurements along airfoil centerline for ice accretion case "g". The thermocouples locations are defined in Figure 4. Since no ice accreted at the midspan leading edge, no ice thickness measurements are presented.

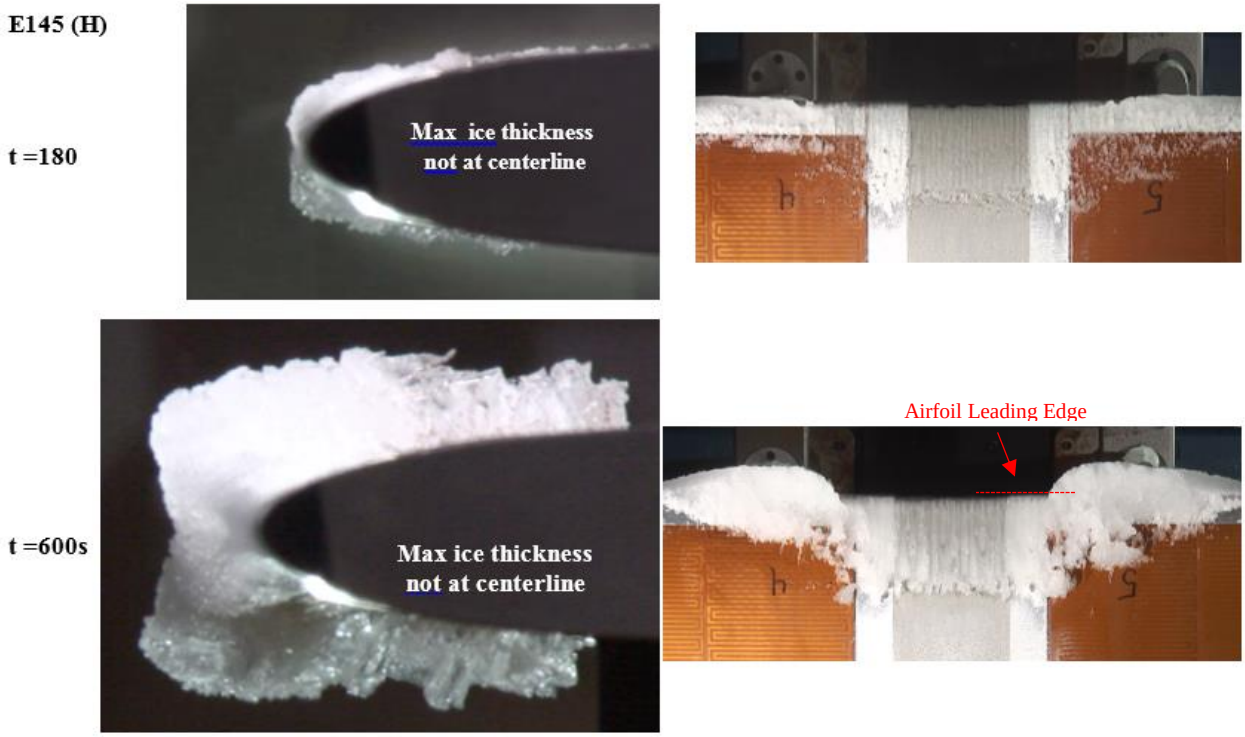

Figure 22. ***Ice Accretion "h":*** *Images after 180 seconds (top row) and 600 seconds (bottom row) of cloud exposure for a plenum relative humidity of ~25% at 135 m/s and MVD_i=50 μ. The left column shows the side view profile and the right column shows a view from above the airfoil. The target aerothermal conditions were $P_{0,i,T}$ = 44.8 kPa (6.5 psia) and $T_{0,i,T}$ = 7.2 ℃ with a static pressure of 40.0 kPa (5.8 psia).*

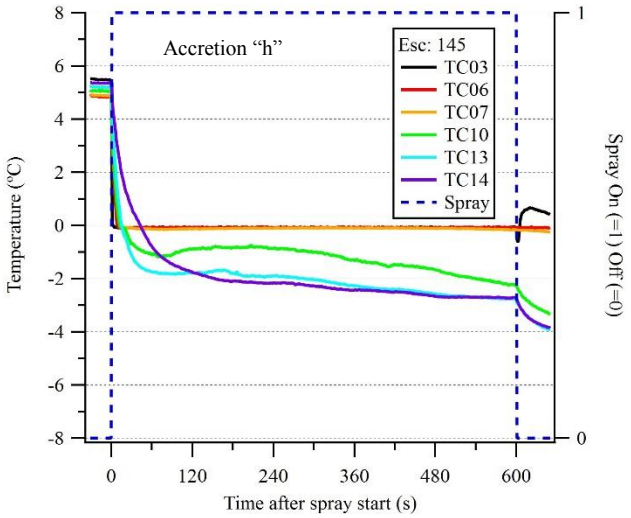

Figure 23. Thermocouple measurements along airfoil centerline for the ice accretion case "h". The thermocouples locations are defined in Figure 4. Since no ice accreted at the midspan leading edge, no ice thickness measurements are presented.

VI. Appendix

The following data tables list the as-run facility conditions and measurements for the test points presented in this paper. In each table, the first column denotes the parameter as defined in the nomenclature section. Column 2 denotes the units while column 3 denotes whether the parameter was a target ("T"), measured ("M"), or calculated ("C") value. Ice accretion data came from the video record. The 8 accretion cases presented in this paper are labeled by their corresponding reference letter "a" – "h", respectively, in the row labelled "Icing". When available, the columns show pairs of tests with the same condition number but performed during different configurations (i.e. configuration 1 with the multiwire and configuration 2 with the airfoil) - these columns have different escort numbers. Columns with escort numbers that include decimal values represent cases where a parameter was varied within that particular test without stopping the spray. For example, escort 85 in Table 4 has three columns. In this test, the relative humidity was varied 3 times. During each change, the measurements were allowed to reach a new steady state before moving to the next relative humidity.

Table 4. Target and as-measured conditions during the 85 m/s and 15 μm relative humidity sweep.

Escort #	Units ↓	Type ↓	59	50	85.3	85.2	85.1	47	123	56	134	70	46
Condition #	(-)	(-)	203.0	205.0	207.8	207.7	207.6	207.0	207.0	208.0	208.0	212.0	211.0
Video #	(-)	(-)	33	26	#N/A	#N/A	#N/A	23	80	30	91	45	22
Configuration	(-)	(-)	1	1	1	1	1	1	2	1	2	1	1
Icing (Y/N)	(-)	(-)	N	N	#N/A	#N/A	#N/A	Y	"a"	N	N	N	N
Target Aerothermal Conditions													
$P_{0,i,T}$	(psia)	T	6.5	6.5	6.5	6.5	6.5	6.5	6.5	6.5	6.5	6.5	6.5
$P_{s,e,T}$	(psia)	T	6.2	6.2	6.2	6.2	6.2	6.2	6.2	6.2	6.2	6.2	6.2
$M_{e,T}$	(-)	T	0.25	0.25	0.25	0.25	0.25	0.25	0.24	0.25	0.24	0.25	0.25
v_T	(m/s)	C	84.7	84.7	84.7	84.7	84.7	84.7	78.7	84.7	78.7	84.7	84.7
$T_{0,i,T}$	(°C)	C	7.2	7.2	7.2	7.2	7.2	7.2	7.2	7.2	7.2	7.2	7.2
$Altitude_T$	(km)	C	6.7	6.7	6.7	6.7	6.7	6.7	6.7	6.7	6.7	6.7	6.7
$RH_{0,i,T}$	(%)	T	20.0	25.0	35.0	38.0	40.0	40.0	40.0	47.1	47.1	54.7	60.0
$\omega_{i,T}$	g/kg	C	2.9	3.6	5.0	5.4	5.7	5.7	5.7	6.8	6.8	7.9	8.6
Aerothermal Measurements & Calculations													
$P_{0,i}$	(psia)	M	6.46	6.46	6.46	6.47	6.46	6.46	6.46	6.46	6.46	6.46	6.46
$P_{s,e}$	(psia)	M	6.20	6.20	6.20	6.20	6.20	6.20	6.19	6.20	6.20	6.21	6.20
P_{tank}	(psia)	M	6.18	6.17	6.18	6.18	6.18	6.18	6.17	6.18	6.18	6.18	6.18
M_e	(-)	M	0.24	0.24	0.24	0.24	0.24	0.24	0.25	0.24	0.24	0.24	0.24
v	(m/s)	M	80.7	80.7	81.5	81.5	81.4	80.6	83.3	80.4	81.6	80.3	80.4
$T_{0,i}$	°C	C	6.7	6.7	7.5	7.4	7.3	6.8	7.2	6.9	6.8	7.4	7.0
$\Delta T_{0,e,c}$	°C	C	-3.9	-3.7	-3.7	-3.8	-4.5	-3.7	-4.4	-4.5	-4.1	-3.2	-2.9
$RH_{0,i}$	(%)	M	19.9	24.5	35.9	37.9	39.3	40.0	40.4	45.3	47.0	56.2	59.6
ω_i	g/kg	M	2.7	3.4	5.2	5.5	5.7	5.6	5.8	6.4	6.5	8.2	8.5
$\Delta\omega_{e,c}$	g/kg	C	2.6	2.2	2.0	1.8	1.5	1.8	1.7	1.5	1.4	1.1	0.9
$\rho_{s,e}$	kg/m3	C	0.54	0.54	0.54	0.54	0.54	0.54	0.54	0.54	0.54	0.54	0.54
ΔGWC_c	g/m3	C	1.4	1.2	1.1	1.0	0.8	1.0	0.9	0.8	0.8	0.6	0.5
$T_{wb,0,e,off}$	(°C)	C	-3.1	-2.4	-0.3	-0.1	0.0	-0.3	0.0	0.5	0.6	2.3	2.5
$T_{wb,s,e,off}$	(°C)	C	-4.7	-4.0	-1.9	-1.7	-1.5	-1.8	-1.5	-1.0	-1.0	0.8	0.9
$T_{wb,s,e,on,c}$	(°C)	C	-3.7	-3.2	-1.4	-1.4	-1.8	-1.6	-1.6	-1.4	-1.2	0.6	0.7
$T_{wb,0,e,on,c}$	(°C)	C	-2.0	-1.6	0.1	0.1	-0.3	-0.1	0.0	0.2	0.3	2.1	2.2
Spray Bar and Water Content Measurements & Calculations													
Nozzles	(-)	M	19	19	0	0	0	19	19	19	19	19	19
$T_{water,i}$	(°C)	M	7.1	7.1	7.2	7.3	7.3	7.1	7.1	7.1	6.7	6.8	7.1
τ	(s)	M	231	362	81	146	85	395	596	289	385	220	646
Q_{noz}	(LPM)	C	3.0	3.0	0.0	0.0	0.0	3.0	3.0	3.0	3.0	3.0	3.0
$P_{water,noz}$	(psig)	M	119.9	119.9	120.0	119.8	119.9	119.9	119.9	119.9	119.9	119.9	119.9
$P_{air,noz}$	(psig)	M	40.4	40.3	40.5	40.1	40.2	40.4	40.4	40.3	40.4	40.2	40.3
ΔP_{noz}	(psid)	M	79.6	79.5	79.5	79.7	79.7	79.5	79.5	79.6	79.5	79.6	79.6
$P_0/(P_0+P_{air,noz})$	(-)	C	0.14	0.14	0.14	0.14	0.14	0.14	0.14	0.14	0.14	0.14	0.14
MVD_i	(um)	T	15	15	15	15	15	15	15	15	15	15	15
Probe 1	(-)	M	CDP	CDP	CDP	CDP	CDP	CDP	CDP	CDP	CDP	CDP	CDP
dv10_Probe 1	μm	M	N/A	N/A	N/A	N/A	N/A	N/A	N/A	N/A	N/A	N/A	N/A
dv50_Probe 1	μm	M	19.90	20.10	#N/A	#N/A	#N/A	19.60	19.60	19.70	19.70	#N/A	19.90
dv90_Probe 1	μm	M	N/A	N/A	N/A	N/A	N/A	N/A	N/A	N/A	N/A	N/A	N/A
Probe 2	(-)	M	N/A	N/A	N/A	N/A	N/A	PDI	PDI	PDI	PDI	N/A	PDI
dv10_Probe 2	μm	M	N/A	N/A	N/A	N/A	N/A	11.39	11.39	11.29	11.29	N/A	12.13
dv50_Probe 2	μm	M	N/A	N/A	N/A	N/A	N/A	20.01	20.01	20.30	20.30	N/A	20.32
dv90_Probe 2	μm	M	N/A	N/A	N/A	N/A	N/A	33.06	33.06	32.61	32.61	N/A	32.77
$TWC_{e,T}$	(g/m3)	C	6.8	6.8	0.0	0.0	0.0	6.8	6.6	6.9	6.8	6.9	6.9
$TWC_{m,IKP2}$	(g/m3)	M	1.28	1.39	1.78	1.84	1.88	2.02	2.02	2.13	2.13	2.38	2.38
$TWC_{m,HP}$	(g/m3)	M	0.97	1.12	1.48	1.43	1.39	1.62	#N/A	1.51	#N/A	1.74	1.84
$LWC_{m,2.1}$	(g/m3)	M	0.08	0.09	0.35	0.80	1.11	0.42	#N/A	1.30	#N/A	1.46	1.59
$LWC_{m,0.5}$	(g/m3)	M	0.09	0.09	0.35	0.75	1.04	0.36	#N/A	1.26	#N/A	1.34	1.50
$CE_{2.1}$	(-)	C	0.90	0.90	0.90	0.90	0.90	0.90	0.90	0.90	0.90	0.90	0.90
$WC_{2.1}$	(-)	C	0.72	0.72	0.72	0.72	0.72	0.72	0.71	0.72	0.72	0.72	0.72
$FR_{2.1}$	(-)	C	0.07	0.07	0.07	0.07	0.07	0.07	0.07	0.07	0.07	0.07	0.07
η_e	(-)	C	0.00	0.01	0.23	0.64	0.89	0.25	N/A	0.92	N/A	0.93	1.02

Table 5. Target and as-measured conditions during the 85 m/s and 50 μm relative humidity sweep.

Escort #	Units ↓	Type ↓	61	139	60	58	127	49	118	48	121	57	45
Condition #	(-)	(-)	201.1	201.1	201.0	202.0	202.0	204.0	204.0	206.0	206.0	209.0	210.0
Video #	(-)	(-)	35 / 36	100	34	32	84	25	75	24	78	31	21
Configuration	(-)	(-)	1	2	1	1	2	1	2	1	2	1	1
Icing (Y/N)	(-)	(-)	Y	"b"	Y	Y	"c"	Y	"d"	Y	"e"	N	N
Target Aerothermal Conditions													
$P_{0,i,T}$	(psia)	T	6.46	6.46	6.46	6.46	6.46	6.46	6.46	6.46	6.46	6.46	6.46
$P_{s,e,T}$	(psia)	T	6.21	6.21	6.21	6.21	6.21	6.21	6.21	6.21	6.21	6.21	6.21
$M_{e,T}$	(-)	T	0.25	0.25	0.25	0.25	0.24	0.25	0.24	0.25	0.24	0.25	0.25
v_T	(m/s)	C	84.72	78.71	84.72	84.72	78.71	84.72	78.71	84.72	78.71	84.72	84.72
$T_{0,i,T}$	(°C)	C	7.2	7.2	7.2	7.2	7.2	7.2	7.2	7.2	7.2	7.2	7.2
$Altitude_T$	(km)	C	6.7	6.7	6.7	6.7	6.7	6.7	6.7	6.7	6.7	6.7	6.7
$RH_{0,i,T}$	(%)	T	1.0	0.0	10.0	20.0	20.0	25.0	25.0	40.0	40.0	47.1	60.0
$\omega_{i,T}$	g/kg	C	0.1	0.0	1.4	2.9	2.9	3.6	3.6	5.7	5.7	6.8	8.6
Aerothermal Measurements & Calculations													
$P_{0,i}$	(psia)	M	6.46	6.46	6.46	6.46	6.46	6.46	6.46	6.46	6.46	6.46	6.46
$P_{s,e}$	(psia)	M	6.21	6.19	6.20	6.20	6.19	6.20	6.18	6.20	6.20	6.20	6.20
P_{tank}	(psia)	M	6.18	6.18	6.18	6.18	6.18	6.17	6.17	6.17	6.18	6.18	6.18
M_e	(-)	M	0.24	0.25	0.24	0.24	0.25	0.24	0.25	0.24	0.24	0.24	0.24
v	(m/s)	M	79.9	82.1	80.2	80.8	82.3	81.0	83.2	81.0	81.4	80.9	80.7
$T_{0,i}$	°C	C	7.0	7.1	7.1	7.0	6.9	6.8	6.9	7.1	6.9	7.2	6.5
$\Delta T_{0,e,c}$	°C	C	-4.0	-4.5	-3.8	-3.6	-4.3	-3.4	-3.8	-3.5	-3.4	-3.5	-2.6
$RH_{0,i}$	(%)	M	0.3	0.1	9.4	18.9	20.0	24.6	24.7	40.1	40.1	47.9	60.8
ω_i	g/kg	M	0.0	0.0	1.3	2.7	2.8	3.4	3.5	5.7	5.6	6.9	8.3
$\Delta\omega_{e,c}$	g/kg	C	2.3	2.3	2.1	1.9	1.8	1.6	1.6	1.3	1.2	1.0	0.8
$\rho_{s,e}$	kg/m3	C	0.54	0.54	0.54	0.54	0.54	0.54	0.54	0.54	0.54	0.54	0.54
ΔGWC_c	g/m3	C	1.2	1.2	1.1	1.0	1.0	0.9	0.8	0.7	0.6	0.6	0.4
$T_{wb,0,e,off}$	(°C)	C	-6.0	-6.0	-4.4	-3.0	-2.9	-2.4	-2.2	-0.1	-0.2	1.1	2.1
$T_{wb,s,e,off}$	(°C)	C	-7.7	-7.9	-6.2	-4.7	-4.6	-4.0	-4.0	-1.6	-1.8	-0.5	0.5
$T_{wb,s,e,on,c}$	(°C)	C	-6.9	-7.2	-5.5	-4.2	-4.6	-3.7	-4.0	-1.7	-2.0	-0.8	0.3
$T_{wb,0,e,on,c}$	(°C)	C	-5.1	-5.3	-3.8	-2.5	-2.8	-2.1	-2.2	-0.1	-0.4	0.7	1.9
Spray Bar and Water Content Measurements & Calculations													
Nozzles	(-)	M	19	19	19	19	19	19	19	19	19	19	19
$T_{water,i}$	(°C)	M	7.1	7.3	7.1	7.1	7.1	7.1	7.0	7.1	7.1	7.1	7.1
τ	(s)	M	277	599	313	288	601	341	179	355	599	295	936
Q_{noz}	(LPM)	C	3.0	3.0	3.0	3.0	3.0	3.0	3.0	3.0	3.0	3.0	3.0
$P_{water,noz}$	(psig)	M	92.9	92.9	92.9	92.9	92.9	92.9	93.0	92.9	92.9	92.9	92.9
$P_{air,noz}$	(psig)	M	13.4	13.4	13.4	13.4	13.3	13.3	13.6	13.3	13.4	13.4	13.3
ΔP_{noz}	(psid)	M	79.5	79.5	79.5	79.6	79.6	79.6	79.4	79.6	79.5	79.5	79.6
$P_0/(P_0+P_{air,noz})$	(-)	C	0.33	0.33	0.33	0.33	0.33	0.33	0.33	0.33	0.33	0.33	0.33
MVD_i	(um)	T	50	50	50	50	50	50	50	50	50	50	50
Probe 1	(-)	M	HSI	HSI	HSI	HSI	HSI	HSI	HSI	HSI	HSI	HSI	HSI
dv10_Probe 1	μm	M	27.68	27.68	27.46	26.36	26.36	25.79	25.79	24.69	24.69	24.85	24.44
dv50_Probe 1	μm	M	51.65	51.65	56.51	49.96	49.96	48.96	48.96	46.90	46.90	47.04	47.41
dv90_Probe 1	μm	M	87.36	87.36	99.10	90.38	90.38	85.68	85.68	89.24	89.24	88.36	97.93
Probe 2	(-)	M	PDI	PDI	PDI	PDI	PDI	PDI	PDI	PDI	PDI	PDI	PDI
dv10_Probe 2	μm	M	25.70	25.70	24.97	26.67	26.67	27.46	27.46	27.03	27.03	27.19	26.22
dv50_Probe 2	μm	M	52.37	52.37	51.77	52.99	52.99	52.34	52.34	53.24	53.24	53.01	52.50
dv90_Probe 2	μm	M	95.93	95.93	92.31	98.92	98.92	96.54	96.54	96.47	96.47	97.48	96.36
$TWC_{e,T}$	(g/m3)	C	6.9	6.7	6.9	6.9	6.7	6.8	6.5	6.8	6.8	6.9	6.9
$TWC_{m,IKP2}$	(g/m3)	M	3.16	3.16	3.49	3.84	3.84	3.87	3.87	4.70	4.70	4.85	5.00
$TWC_{m,HP}$	(g/m3)	M	1.89	#N/A	2.24	2.69	#N/A	3.33	#N/A	3.70	#N/A	4.05	4.29
$LWC_{m,2.1}$	(g/m3)	M	0.45	#N/A	0.60	0.95	#N/A	1.12	#N/A	2.70	#N/A	2.77	3.19
$LWC_{m,0.5}$	(g/m3)	M	0.40	#N/A	0.52	0.79	#N/A	0.87	#N/A	1.85	#N/A	2.24	2.22
$CE_{2.1}$	(-)	C	0.98	0.98	0.98	0.98	0.98	0.98	0.98	0.98	0.98	0.98	0.98
$WC_{2.1}$	(-)	C	0.66	0.65	0.66	0.65	0.65	0.65	0.64	0.65	0.65	0.65	0.65
$FR_{2.1}$	(-)	C	0.07	0.07	0.07	0.07	0.07	0.07	0.07	0.07	0.07	0.07	0.07
η_e	(-)	C	0.14	N/A	0.19	0.31	N/A	0.39	N/A	0.89	N/A	0.88	0.99

Table 6. Target and as-measured conditions during the 135 m/s and 15 µm relative humidity sweep.

Escort #	Units ↓	Type ↓	91		101		93.1	93.2	93.3	92	149	94	
Condition #	(-)	(-)	305.0		326.0		307.2	307.3	307.4	307.0	307.0	308.0	
Video #	(-)	(-)	51		61		#N/A	#N/A	#N/A	52	111	54	
Configuration	(-)	(-)	1		1		1	1	1	1	2	1	
Icing (Y/N)	(-)	(-)	N		#N/A		#N/A	#N/A	#N/A	Y	"f"	Y	
Target Aerothermal Conditions													
$P_{0,i,T}$	(psia)	T	6.5		6.5		6.5	6.5	6.5	6.47	6.47	6.5	
$P_{s,e,T}$	(psia)	T	5.8		5.8		5.8	5.8	5.8	5.79	5.79	5.8	
$M_{e,T}$	(-)	T	0.41		0.41		0.41	0.41	0.41	0.41	0.41	0.41	
v_T	(m/s)	C	135.0		135.0		135.0	135.0	135.0	135.0	135.0	135.0	
$T_{0,i,T}$	(°C)	C	7.2		7.2		7.2	7.2	7.2	7.2	7.2	7.2	
$Altitude_T$	(km)	C	7.2		7.2		7.2	7.2	7.2	7.2	7.2	7.2	
$RH_{0,i,T}$	(%)	T	25.0		25.0		33.0	36.0	38.0	40.0	40.0	50.0	
$\omega_{i,T}$	g/kg	C	3.6		3.6		4.7	5.1	5.4	5.7	5.7	7.2	
Aerothermal Measurements & Calculations													
$P_{0,i}$	(psia)	M	6.5		6.5		6.5	6.5	6.5	6.5	6.5	6.5	
$P_{s,e}$	(psia)	M	5.8		5.8		5.8	5.8	5.8	5.8	5.8	5.8	
P_{tank}	(psia)	M	5.8		5.8		5.8	5.8	5.8	5.8	5.8	5.8	
M_e	(-)	M	0.39		0.39		0.39	0.39	0.39	0.39	0.40	0.39	
v	(m/s)	M	127.9		127.3		127.8	128.2	128.5	128.3	130.9	128.5	
$T_{0,i}$	°C	C	6.8		6.8		7.0	7.1	7.1	7.1	7.0	7.4	
$\Delta T_{0,e,c}$	°C	C	-7.6		-7.3		-6.3	-6.3	-5.9	-6.0	-5.9	-4.6	
$RH_{0,i}$	(%)	M	25.0		25.1		33.0	36.0	37.8	40.2	40.9	50.6	
ω_i	g/kg	M	3.5		3.5		4.7	5.1	5.4	5.7	5.8	7.3	
$\Delta\omega_{e,c}$	g/kg	C	2.3		2.5		1.9	1.7	1.6	1.7	1.6	1.1	
$\rho_{s,e}$	kg/m3	C	0.52		0.52		0.52	0.52	0.52	0.52	0.51	0.51	
ΔGWC_c	g/m3	C	1.2		1.3		1.0	0.9	0.8	0.9	0.8	0.6	
$T_{wb,0,e,off}$	(°C)	C	-2.3		-2.3		-1.0	-0.6	-0.3	0.0	-0.1	1.6	
$T_{wb,s,e,off}$	(°C)	C	-6.5		-6.4		-5.0	-4.6	-4.3	-3.9	-4.1	-2.3	
$T_{wb,s,e,on,c}$	(°C)	C	-7.4		-6.9		-5.7	-5.4	-5.1	-4.7	-4.9	-3.0	
$T_{wb,0,e,on,c}$	(°C)	C	-3.1		-2.8		-1.6	-1.4	-1.1	-0.7	-0.8	0.9	
Spray Bar and Water Content Measurements & Calculations													
Nozzles	(-)	M	22		22		0	0	0	22	22	22	
$T_{water,i}$	(°C)	M	7.3		6.8		7.3	7.3	7.3	7.3	7.0	7.3	
τ	(s)	M	197		132		118	128	114	134	599	224	
Q_{noz}	(LPM)	C	4.7		4.7		0.0	0.0	0.0	4.7	4.7	4.7	
$P_{water,noz}$	(psig)	M	80.0		79.9		79.9	79.9	80.0	79.8	79.9	80.0	
$P_{air,noz}$	(psig)	M	59.6		59.6		59.6	59.6	59.6	59.5	59.7	59.6	
ΔP_{noz}	(psid)	M	20.4		20.3		20.3	20.3	20.4	20.4	20.2	20.3	
$P_0/(P_0+P_{air,noz})$	(-)	C	0.10		0.10		0.10	0.10	0.10	0.10	0.10	0.10	
MVD_i	(um)	T	15		15		15	15	15	15	15	15	
Probe 1	(-)	M	CDP		CDP		CDP	CDP	CDP	CDP	CDP	CDP	
dv10_Probe 1	µm	M	N/A		N/A		N/A	N/A	N/A	N/A	N/A	N/A	
dv50_Probe 1	µm	M	#N/A		#N/A		#N/A	#N/A	#N/A	20.70	20.70	#N/A	
dv90_Probe 1	µm	M	N/A		N/A		N/A	N/A	N/A	N/A	N/A	N/A	
Probe 2	(-)	M	N/A		N/A		N/A	N/A	N/A	PDI	PDI	N/A	
dv10_Probe 2	µm	M	N/A		N/A		N/A	N/A	N/A	11.93	11.93	N/A	
dv50_Probe 2	µm	M	N/A		N/A		N/A	N/A	N/A	18.79	18.79	N/A	
dv90_Probe 2	µm	M	N/A		N/A		N/A	N/A	N/A	28.28	28.28	N/A	
$TWC_{e,T}$	(g/m3)	C	6.8		6.8		0.0	0.0	0.0	6.8	6.7	6.8	
$TWC_{m,IKP2}$	(g/m3)	M	2.33		N/A		2.72	2.87	2.96	3.05	3.05	3.63	
$TWC_{m,HP}$	(g/m3)	M	2.20		2.17		2.40	2.55	2.61	2.35	#N/A	2.53	
$LWC_{m,2.1}$	(g/m3)	M	0.29		0.29		0.33	0.45	0.64	1.86	#N/A	2.06	
$LWC_{m,0.5}$	(g/m3)	M	0.34		0.33		0.40	0.50	0.68	1.75	#N/A	1.93	
$CE_{2.1}$	(-)	C	0.92		0.92		0.92	0.92	0.92	0.92	0.92	0.92	
$WC_{2.1}$	(-)	C	0.61		0.61		0.61	0.61	0.61	0.61	0.60	0.61	
$FR_{2.1}$	(-)	C	0.13		0.13		0.13	0.13	0.13	0.13	0.14	0.13	
η_e	(-)	C	0.00		N/A		-0.01	0.07	0.21	1.10	N/A	1.01	

Table 7. Target and as-measured conditions during the 135 m/s and 50 μm relative humidity sweep.

Escort #	Units ↓	Type ↓	87	143	88	145	89		90
Condition #	(-)	(-)	301.0	301.0	304.0	304.0	309.0	309.0	310.0
Video #	(-)	(-)	47	104	48	106	49	109	50
Configuration	(-)	(-)	1	2	1	2	1	2	1
Icing (Y/N)	(-)	(-)	Y	"g"	Y	"h"	Y	N	N
Target Aerothermal Conditions									
$P_{0,i,T}$	(psia)	T	6.5	6.5	6.5	6.5	6.5	6.5	6.5
$P_{s,e,T}$	(psia)	T	5.8	5.8	5.8	5.8	5.8	5.8	5.8
$M_{e,T}$	(-)	T	0.41	0.41	0.41	0.41	0.41	0.41	0.41
v_T	(m/s)	C	135.0	135.0	135.0	135.0	135.0	135.0	135.0
$T_{0,i,T}$	(°C)	C	7.2	7.2	7.2	7.2	7.2	7.2	7.2
$Altitude_T$	(km)	C	7.2	7.2	7.2	7.2	7.2	7.2	7.2
$RH_{0,i,T}$	(%)	T	10.0	10.0	25.0	25.0	50.0	50.0	60.0
$\omega_{i,T}$	g/kg	C	1.4	1.4	3.6	3.6	7.2	7.2	8.6
Aerothermal Measurements & Calculations									
$P_{0,i}$	(psia)	M	6.5	6.5	6.5	6.5	6.5	6.5	6.5
$P_{s,e}$	(psia)	M	5.8	5.8	5.8	5.8	5.8	5.8	5.8
P_{tank}	(psia)	M	5.8	5.8	5.8	5.8	5.8	5.8	5.8
M_e	(-)	M	0.39	0.40	0.39	0.40	0.39	0.40	0.39
v	(m/s)	M	128.4	131.9	128.1	131.9	128.2	132.4	128.5
$T_{0,i}$	°C	C	7.0	7.3	7.5	7.4	6.9	7.3	7.6
$\Delta T_{0,e,c}$	°C	C	-4.6	-6.4	-4.4	-5.4	-2.9	-4.2	-3.0
$RH_{0,i}$	(%)	M	9.8	9.7	25.5	25.4	48.8	50.7	58.3
ω_i	g/kg	M	1.4	1.4	3.7	3.7	6.8	7.3	8.6
$\Delta\omega_{e,c}$	g/kg	C	1.6	2.0	1.3	1.4	0.8	0.7	0.4
$\rho_{s,e}$	kg/m3	C	0.52	0.51	0.51	0.51	0.52	0.51	0.51
ΔGWC_c	g/m3	C	0.8	1.0	0.7	0.7	0.4	0.3	0.2
$T_{wb,0,e,off}$	(°C)	C	-4.4	-4.2	-1.8	-1.9	1.0	1.5	2.7
$T_{wb,s,e,off}$	(°C)	C	-8.9	-9.0	-5.9	-6.3	-2.9	-2.6	-1.1
$T_{wb,s,e,on,c}$	(°C)	C	-9.2	-9.7	-6.4	-7.1	-3.2	-3.6	-1.8
$T_{wb,0,e,on,c}$	(°C)	C	-4.7	-4.8	-2.3	-2.6	0.6	0.6	2.1
Spray Bar and Water Content Measurements & Calculations									
Nozzles	(-)	M	22	22	22	22	22	22	22
$T_{water,i}$	(°C)	M	7.3	7.3	7.3	7.2	7.3	7.0	7.3
τ	(s)	M	233	600	236	600	184	245	187
Q_{noz}	(LPM)	C	4.7	4.7	4.7	4.7	4.7	4.7	4.7
$P_{water,noz}$	(psig)	M	31.9	31.9	31.9	31.9	31.9	31.9	31.9
$P_{air,noz}$	(psig)	M	11.7	11.7	11.9	11.8	11.9	11.9	11.8
ΔP_{noz}	(psid)	M	20.2	20.2	20.0	20.1	20.0	20.0	20.1
$P_0/(P_0+P_{air,noz})$	(-)	C	0.35	0.35	0.35	0.35	0.35	0.35	0.35
MVD_i	(um)	T	50	50	50	50	50	50	50
Probe 1	(-)	M	HSI	HSI	HSI	HSI	HSI	HSI	HSI
dv10_Probe 1	μm	M	26.85	26.85	26.88	26.88	26.77	26.77	#N/A
dv50_Probe 1	μm	M	48.16	48.16	45.51	45.51	44.31	44.31	#N/A
dv90_Probe 1	μm	M	95.12	95.12	75.43	75.43	83.76	83.76	#N/A
Probe 2	(-)	M	N/A	N/A	N/A	N/A	N/A	N/A	N/A
dv10_Probe 2	μm	M	N/A	N/A	N/A	N/A	N/A	N/A	N/A
dv50_Probe 2	μm	M	N/A	N/A	N/A	N/A	N/A	N/A	N/A
dv90_Probe 2	μm	M	N/A	N/A	N/A	N/A	N/A	N/A	N/A
$TWC_{e,T}$	(g/m3)	C	6.8	6.6	6.8	6.6	6.8	6.5	6.8
$TWC_{m,IKP2}$	(g/m3)	M	6.59	6.59	6.99	6.99	8.15	8.15	8.24
$TWC_{m,HP}$	(g/m3)	M	4.10	#N/A	4.69	#N/A	5.42	#N/A	6.11
$LWC_{m,2.1}$	(g/m3)	M	1.77	#N/A	2.44	#N/A	3.61	#N/A	3.86
$LWC_{m,0.5}$	(g/m3)	M	1.35	#N/A	1.52	#N/A	1.94	#N/A	2.01
$CE_{2.1}$	(-)	C	0.99	0.99	0.99	0.99	0.99	0.99	0.99
$WC_{2.1}$	(-)	C	0.48	0.47	0.48	0.47	0.48	0.46	0.48
$FR_{2.1}$	(-)	C	0.13	0.14	0.13	0.14	0.13	0.14	0.13
η_e	(-)	C	0.40	N/A	0.64	N/A	0.91	N/A	0.99